FEDERAL UNIVERSITY OF CEARÁ

CENTER OF SCIENCES

DEPARTMENT OF ANALYTICAL AND PHYSICAL CHEMISTRY

GRADUATE PROGRAM IN CHEMISTRY

EDNARA JOICE BRAGA

SYNTHESIS AND CHARACTERIZATION OF A HYBRID PEROVSKITE WITH AN IMIDAZOLE SPACER FOR OPTOELECTRONIC APPLICATIONS

FORTALEZA

2025

EDNARA JOICE BRAGA

SYNTHESIS AND CHARACTERIZATION OF A HYBRID PEROVSKITE WITH AN IMIDAZOLE SPACER FOR OPTOELECTRONIC APPLICATIONS

Dissertation submitted to the Graduate Program in Chemistry at the Federal University of Ceará, in partial fulfillment of the requirements for the degree of Master of Science in Chemistry. Concentration area: Chemistry.
Advisor: Prof. Dr. Pierre Basílio Almeida Fechine.
Co-advisor: Prof. Dr. Davino Machado Andrade Neto.

FORTALEZA
2025

EDNARA JOICE BRAGA

SYNTHESIS AND CHARACTERIZATION OF A HYBRID PEROVSKITE WITH AN IMIDAZOLE SPACER FOR OPTOELECTRONIC APPLICATIONS

Dissertation submitted to the Graduate Program in Chemistry at the Federal University of Ceará, in partial fulfillment of the requirements for the degree of Master of Science in Chemistry. Concentration area: Chemistry.
Advisor: Prof. Dr. Pierre Basílio Almeida Fechine.
Co-advisor: Prof. Dr. Davino Machado Andrade Neto.

Approved on: 25/08/2025.

EXAMINING COMMITTEE

_____
Prof. Dr. Pierre Basílio Almeida Fechine (Advisor)
Federal University of Ceará (UFC)

_____
Prof. Dr. Davino Machado Andrade Neto (Co-advisor)
Federal University of Ceará (UFC)

_____
Prof. Dr. Alejandro Pedro Ayala
Federal University of Ceará (UFC)

_____
Prof. Dr. Samuel Veloso Carneiro
Federal University of Ceará (UFC)

A Deus.

Aos meus pais, Eduardo Jorge Braga e Maria Ruberlene Salvador.

ACKNOWLEDGEMENTS

I would like to thank the Coordination for the Improvement of Higher Education Personnel – Brazil (CAPES) for the financial support granted through a scholarship within the scope of the Graduate Program at the Federal University of Ceará (UFC). This study was funded by CAPES – Funding Code 001, as established by Ordinance No. 206, of September 4, 2018.

To my advisor, Prof. Dr. Pierre Basilio Almeida Fechine, I express my gratitude for his solid guidance, scientific contributions, and trust throughout the development of this work.

To my co-advisor and friend, Prof. Dr. Davino Machado Andrade Neto, I am grateful for his close involvement since the early stages of this work, his availability, and his constant technical support.

I also thank my colleagues and professors from the GQMAT Research Group (Advanced Materials Chemistry Group) for the knowledge exchange, constructive discussions, and collaboration throughout this academic journey.

I extend my sincere gratitude to the Structural Crystallography Group for the support, discussions, and access to essential infrastructure, which were fundamental for the analysis of the materials studied in this work.

Finally, I thank the Department of Physics at the Federal University of Ceará for the academic environment, institutional support, and resources that greatly contributed to the realization of this work.

RESUMO

As perovskitas constituem um grupo de materiais emergentes que têm atraído interesse na comunidade científica devido às suas propriedades semicondutoras. Perovskitas tridimensionais híbridas apresentam bom desempenho em dispositivos optoeletrônicos, como células solares e diodos emissores de luz (LEDs). A predominância do uso de íons chumbo (Pb^{2+}) na constituição de perovskitas, embora eficaz em termos de eficiência, levanta preocupações quanto a sua toxicidade e a sua limitada estabilidade em condições ambiente. Nesse cenário, o estanho (Sn) tem se destacado como um substituto promissor para o chumbo (Pb), reduzindo a toxicidade sem comprometer o desempenho. Além da substituição do Pb por Sn a incorporação de novos cátions orgânicos na constituição de perovskitas híbridas tem sido apontado como alternativa promissora para melhoria na estabilidade de perovskitas materiais. Essa modificação leva à formação de haletos metálicos híbrido orgânico-inorgânicos, que aumentam a estabilidade química do material, além de influenciar suas propriedades estruturais e eletrônicas. Neste trabalho, a perovskita híbrida $(C_{11}H_{11}N_2O)_2SnBr_6$ foi sintetizada por meio da metodologia de evaporação lenta em meio ácido. A estrutura incorpora como cátion orgânico a molécula 2-(1H-imidazol-1-il)-1-feniletanona, enquanto o Sn^{4+} coordena seis átomos de bromo, formando o octaedro $[SnBr_6]^{2-}$. A organização cristalina resultante caracteriza-se como uma perovskita de dimensionalidade zero (0D), composta por unidades octaédricas isoladas. O composto apresenta emissão de banda larga, abrangendo grande parte do espectro visível. Essa característica é associada à recombinação radiativa de éxcitons autoaprisionados (STE), um fenômeno comum em perovskitas híbridas de haleto. Além da sua estabilidade, que é um fator determinante para aplicações práticas, a perovskita exibe um bandgap óptico de 2,99 eV, um valor que torna esse composto um potencial candidato para aplicações em dispositivos optoeletrônicos. Dessa forma, a pesquisa contribui para o desenvolvimento de materiais alternativos que não só oferecem desempenho competitivo em relação às perovskitas convencionais à base de chumbo, mas também mitigam os desafios de sustentabilidade e toxicidade, ampliando as possibilidades de aplicações tecnológicas seguras e eficazes.

Palavras-chave: perovskita híbrida de estanho; semicondutores; optoeletrônicos.

ABSTRACT

Perovskites are an emerging class of materials that have attracted significant attention from the scientific community due to their semiconductor properties. Three-dimensional hybrid perovskites demonstrate good performance in optoelectronic devices, such as solar cells and light-emitting diodes (LEDs). The predominant use of lead ions (Pb^{2+}) in the composition of perovskites, although effective in terms of efficiency, raises concerns related to toxicity and limited stability under ambient conditions. In this context, tin (Sn) has emerged as a promising substitute for lead, reducing toxicity without compromising performance. In addition to replacing Pb with Sn, the incorporation of novel organic cations into the structure of hybrid perovskites has been considered a promising strategy to improve their chemical and environmental stability. This modification leads to the formation of hybrid organic-inorganic metal halides, which enhance the structural integrity and influence the electronic and optical properties of the material. In this work, the hybrid perovskite $(C_{11}H_{11}N_2O)_2SnBr_6$ was synthesized using a slow evaporation method in an acidic medium. The structure incorporates the organic cation 2-(1H-imidazol-1-yl)-1-phenylethanone, while Sn^{4+} coordinates six bromide atoms, forming the $[SnBr_6]^{2-}$ octahedron. The resulting crystalline organization is classified as a zero-dimensional (0D) perovskite, composed of isolated octahedral units. The compound exhibits broad-band emission across a large portion of the visible spectrum. This feature is associated with the radiative recombination of self-trapped excitons (STEs), a phenomenon commonly observed in hybrid halide perovskites. In addition to its structural stability, a key factor for practical applications, the perovskite displays a direct optical bandgap of 2.99 eV, making it a potential candidate for optoelectronic devices. Thus, this research contributes to the development of alternative materials that not only offer competitive performance compared to conventional lead-based perovskites but also address challenges related to sustainability and toxicity, broadening the scope for safe and efficient technological applications.

Keywords: tin-based hybrid perovskite; semiconductors; optoelectronics.

LIST OF FIGURES

LIST OF ABBREVIATIONS AND ACRONYMS

0D	Zero-dimensional
3D	Three-dimensional
AFM	Atomic Force Microscopy
CAPES	Coordination for the Improvement of Higher Education Personnel
CBM	Conduction Band Minimum
CIE	Commission Internationale de l'Éclairage
DFT	Density Functional Theory
DRS	Diffuse Reflectance Spectroscopy
Eg	Bandgap
FTIR	Fourier Transform Infrared Spectroscopy
FWHM	Full Width at Half Maximum
IEA	International Energy Agency
ISES	International Solar Energy Society
LED	Light-Emitting Diode
LNLS	Brazilian Synchrotron Light Laboratory
NREL	National Renewable Energy Laboratory
PL	Photoluminescence
PSC	Perovskite Solar Cell
SCXRD	Single-Crystal X-ray Diffraction
SEM	Scanning Electron Microscopy
STE	Self-Trapped Exciton
TCSPC	Time-Correlated Single Photon Counting
TEM	Transmission Electron Microscopy
UFC	Federal University of Ceará
VBM	Valence Band Maximum

TABLE OF CONTENTS

1 INTRODUCTION

Population growth and economic development have led to a significant increase in global energy demand (INTERNATIONAL ENERGY AGENCY, 2024). In emerging and developing economies, which account for approximately 85% of the world's population, this demand has grown at a rate of about 2.6% per year over the past decade. The accelerated pace of development has amplified the need for cleaner energy sources to replace dependence on oil, gas, and coal (UNITED NATIONS, 2025).

Currently, the use of fossil fuels remains the main contributor to greenhouse gas emissions, accounting for more than 75% of such emissions. However, the share of fossil fuels in the global energy mix has declined, from 82% in 2013 to 80% in 2023. Meanwhile, renewable sources are gaining ground, meeting 40% of the growth in energy demand and already representing approximately 29% of global electricity generation (UNITED NATIONS, 2025). This scenario highlights the urgent need to invest in alternative energy sources that are clean, accessible, sustainable, and reliable. Increasing the share of renewable energies, especially in emerging markets, will be crucial to achieving a global energy transition. Although moving towards a more sustainable energy system is more challenging in these economies, where population and industrial growth are faster, the role of clean energy becomes even more important to ensure a sustainable future that is less dependent on fossil fuels (INTERNATIONAL ENERGY AGENCY, 2024; WANG; WANG, 2020).

Among the various renewable energy sources, photovoltaic technology is recognized as one of the most promising options to meet the future needs of society, offering a clean and sustainable solution to the challenge of global energy scarcity (LIANG et al., 2025; LIU et al., 2025). According to the International Solar Energy Society (ISES), solar photovoltaic and wind energy sources are being deployed at a rate five times higher than the combined total of all other operational electricity generation sources. This scenario provides empirical evidence that both technologies stand out as economically competitive and technically viable alternatives for expanding global electricity generation capacity. Figure 1 illustrates the annual net additions of global electricity generation capacity from non-fossil sources between 2021 and 2024, highlighting the remarkable growth of solar photovoltaic energy compared to other renewable sources such as wind, hydro, and nuclear. The accelerated expansion of solar energy reinforces its position as the technology with the greatest potential to drive the energy transition, ensuring a rapid increase in installed capacity on a global scale (PV Magazine Brasil, 2025). According to the latest report by the International Energy Agency

(IEA), solar energy is expected to surpass traditional sources such as nuclear, wind, hydro, gas, and coal, becoming the world's primary source of electricity by 2033. This growth is driven primarily by the increase in installed capacity in countries such as China, the United States, and India, which have made massive investments in solar infrastructure and incentive policies to accelerate the energy transition (INTERNATIONAL ENERGY AGENCY, 2024).

Figure 1 – Annual net additions of global electricity generation capacity from non-fossil sources (2021–2024).

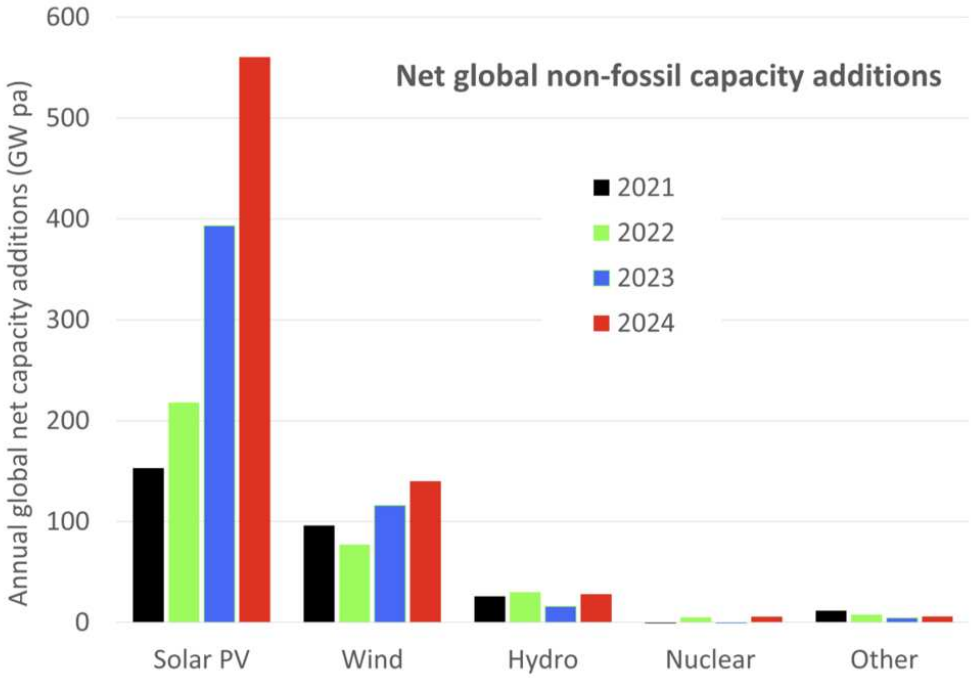

Source: ISES, adapted.

With the rapid advancement of photovoltaic energy, over the past 50 years, new methods for converting light energy through photoelectrochemical cells have been widely investigated, employing various combinations of inorganic semiconductors, organic sensitizers, and other materials (KOJIMA et al., 2009). Among these approaches, perovskite solar cells have stood out, showing significant progress over the past decade. This evolution in the field is accompanied by a substantial increase in the number of scientific publications related to perovskites, as evidenced in Figure 2, which presents the annual growth of indexed articles on the subject. This trend is attributed not only to the intrinsic properties of perovskites, such as the possibility of tuning the optical bandgap through compositional modulation, high charge carrier mobility, relatively long recombination times (which favor efficient charge separation), and a high absorption coefficient in the visible range, but also to technical advances achieved

in synthesis methods, compositional engineering, and device interface optimization (LIANG et al., 2025). These improvements position perovskites as strong candidates to compete with conventional crystalline silicon solar cells in the market in the near future (MIAH et al., 2024; ZHONG et al., 2022).

Figure 2 – Annual evolution of the number of scientific publications related to perovskites.

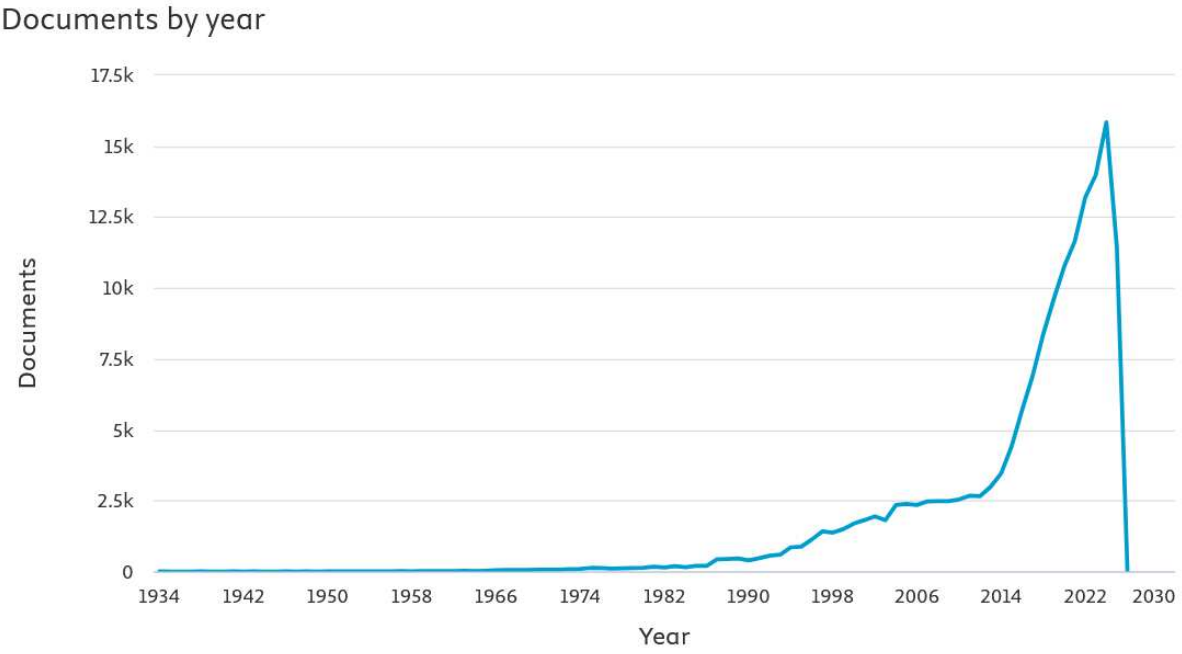

Source: SCOPUS - Elsevier (2025).

Perovskite-based materials constitute an emerging class of semiconductors with relevant applications in optoelectronic devices (LIN et al., 2018). In particular, the development of low-dimensional organic–inorganic hybrid perovskites has advanced significantly, being explored in areas such as solar cells (LIU et al., 2025) and light-emitting diode (LED) technology (VASHISHTHA et al., 2019).

Halide perovskites possess a crystal structure that combines organic or inorganic cations, metal ions such as Pb^{2+}, Sn^{4+}, Bi^{3+}, and halides (Cl^{-}, Br^{-}, or I^{-}) in their arrangement (RAINA et al., 2025). However, the presence of Pb in their composition imparts a harmful nature, posing environmental and health risks, in addition to limited stability under adverse conditions such as humidity, heat, and light exposure. Numerous investigations have addressed the substitution of Pb ions in perovskites, suggesting alternative elements based on similarities in size, charge, chemical reactivity, and properties. The most promising approach involves replacing Pb with other group 14 elements, such as Sn and/or Ge (SOARES et al., 2024).

In addition to reducing the environmental impacts associated with the use of toxic materials, tin-based perovskites also exhibit relevant optoelectronic properties, making them technically suitable for integration into light energy conversion and emission devices (FERJANI et al., 2025). These perovskites stand out for having narrower bandgaps, high absorption coefficients, and elevated mobilities for both holes and electrons compared to lead-based perovskites (ZANNATUL ARIF; ZHOU, 2025).

The possibility of varying organic ligands also allows for the adjustment of the structural dimensionality of these materials, directly influencing their optoelectronic properties and applicability in different systems (FERJANI et al., 2025). Such tuning of the molecular structure can result in materials with customized properties to meet specific demands for efficiency and stability (DALPIAN et al., 2018).

To overcome the limitations of traditional perovskites, particularly their instability and the environmental impacts associated with the use of toxic metals, this work proposes the development of a vacancy-ordered double perovskite based on tin and bromine, containing a functionalized organic cation. This approach aims to combine structural stability and suitable optoelectronic properties through the formation of a hybrid organic–inorganic network. Figure 3 shows the chemical structure of the organic cation used in the synthesis of the proposed perovskite.

Figure 3 – Chemical structure of the organic cation 2-(1H-imidazol-1-yl)-1-phenylethanone.

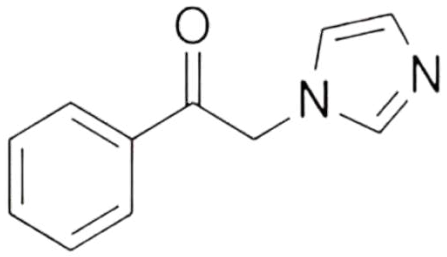

Source: Prepared by the author.

The adopted molecular design strategy is based on two essential principles that complement each other in stabilizing and modulating the material's properties. The inclusion of the ketone functional group aims to enhance intermolecular interactions between organic molecules and to promote interactions between the organic molecule and the inorganic octahedra. As demonstrated by Zhang et al. (2024), the use of molecules with polar groups contributes to the passivation of surface defects, which can assist in stabilizing the tin-based

structure. In parallel, the incorporation of the imidazole group, whose application is scarcely explored in the literature, shows potential for modulating the electronic properties of the system. According to Im et al. (2016), the presence of imidazole can alter the electronic distribution of the cation, influencing the interaction between organic and inorganic units and, consequently, the electronic properties of the perovskite. Figure 4 illustrates the crystal structure of the hybrid perovskite $(C_{11}H_{11}N_2O)_2SnBr_6$, highlighting the isolated $[SnBr_6]^{2-}$ octahedra and the arrangement of the surrounding organic cations. The synthesis of the proposed crystal, which combines both functionalities, has not yet been reported in the literature and represents a new alternative for applications in optoelectronic devices.

Figure 4 – Representation of the hybrid perovskite $(C_{11}H_{11}N_2O)_2SnBr_6$.

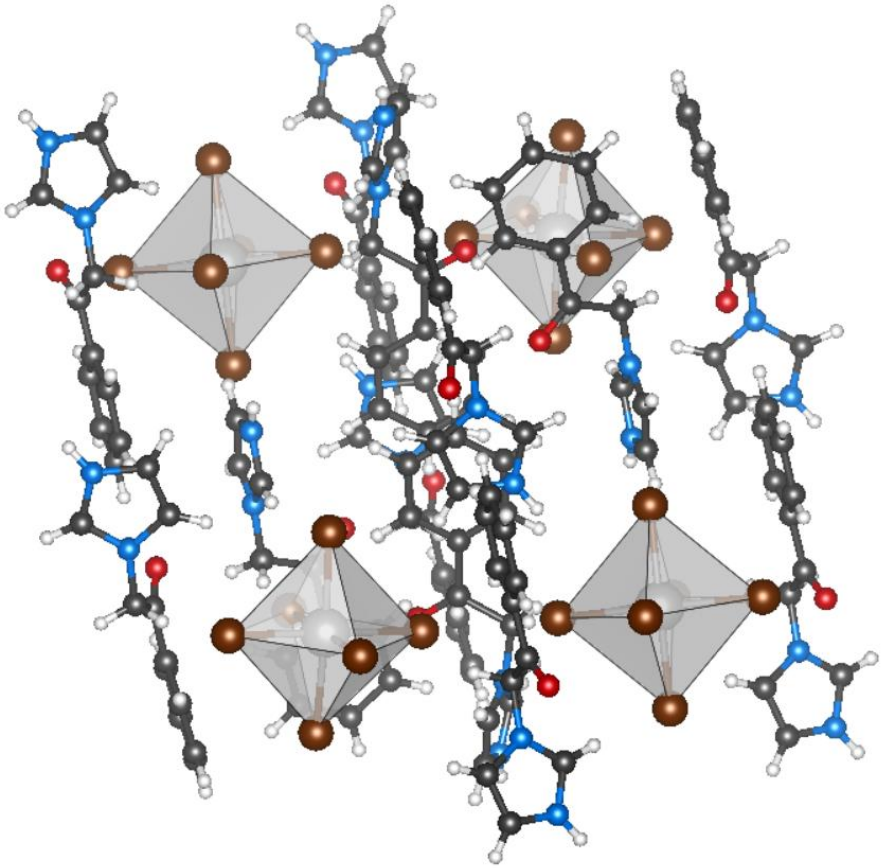

Source: Prepared by the author.

2 OBJECTIVES

2.1 General Objective

To characterize a new low-dimensional hybrid perovskite, $(C_{11}H_{11}N_2O)_2SnBr_6$, aiming at its application in high-efficiency and high-stability optoelectronic devices, as an alternative to conventional lead-based perovskites.

2.2 Specific Objectives

- To synthesize the $(C_{11}H_{11}N_2O)_2SnBr_6$ perovskite crystals;
- To elucidate the crystal structure of the obtained material based on single-crystal X-ray diffraction (SCXRD) data;
- To characterize the optical properties of the compound, with emphasis on absorption in the visible range, photoluminescence emission at different temperatures, and determination of emission lifetime;
- To analyze the molecular vibrations of the system based on FTIR and Raman spectra.

3 LITERATURE REVIEW

3.1 Structure and Properties of Perovskites

Perovskites refer to a class of materials whose structures are derived from the mineral $CaTiO_3$, described by Gustav Rose in 1839. These materials exhibit a typical crystal structure represented by the general formula ABX_3 (Figure 5), in which the A cation occupies the vertices of the unit cell, the B cation is located at the center of an octahedron formed by six X anions, which are positioned at the centers of the cell faces and at the vertices of the octahedron. This three-dimensional configuration results in a network of $[BX_6]$ octahedra interconnected by corner-sharing. The structural arrangement endows perovskites with a combination of electronic, optical, and structural properties that favor their application in various technological devices, such as solar cells, LEDs, and optical sensors (GIORGI; YAMASHITA, 2015).

Figure 5 – Schematic representation of the structure of an ABX_3 perovskite.

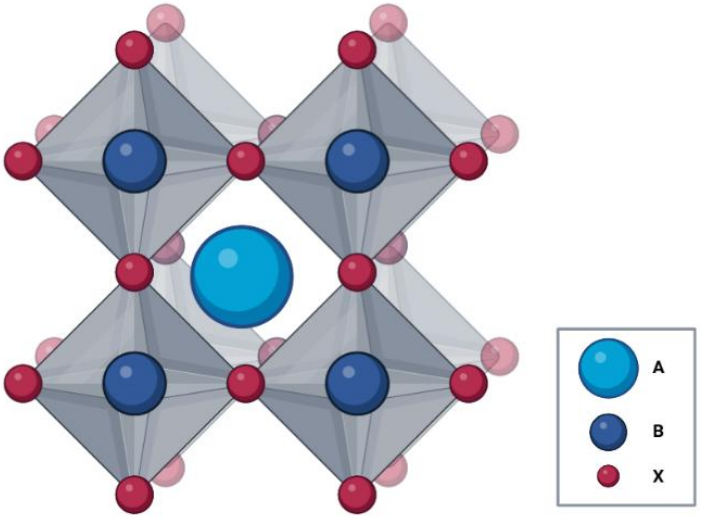

Source: Prepared by the author.

The search for new structural architectures and the improvement of optoelectronic properties has driven the development of organic–inorganic hybrid perovskites. In these structures, the inorganic monovalent cation (such as Cs^+), traditionally present at the A-site of the ABX_3 structure, is replaced by molecular organic cations, such as methylammonium (MA^+), formamidinium (FA^+), or tetramethylammonium (TMA^+). The chemical structures of these cations are illustrated in Figure 6. This substitution introduces greater chemical and structural

flexibility to the material, allowing adjustments in dimensionality, bandgap width, and thermal and environmental stability. As a result, these hybrid perovskites exhibit tunable properties that make them suitable for applications in solar cells, LEDs, and other advanced optoelectronic devices (GIORGI; YAMASHITA, 2015; LIU et al., 2021).

Figure 6 – Chemical structures of cations commonly used at the A-site of hybrid perovskites: Cs^+ ions (inorganic), methylammonium (MA^+), formamidinium (FA^+), and tetramethylammonium (TMA^+).

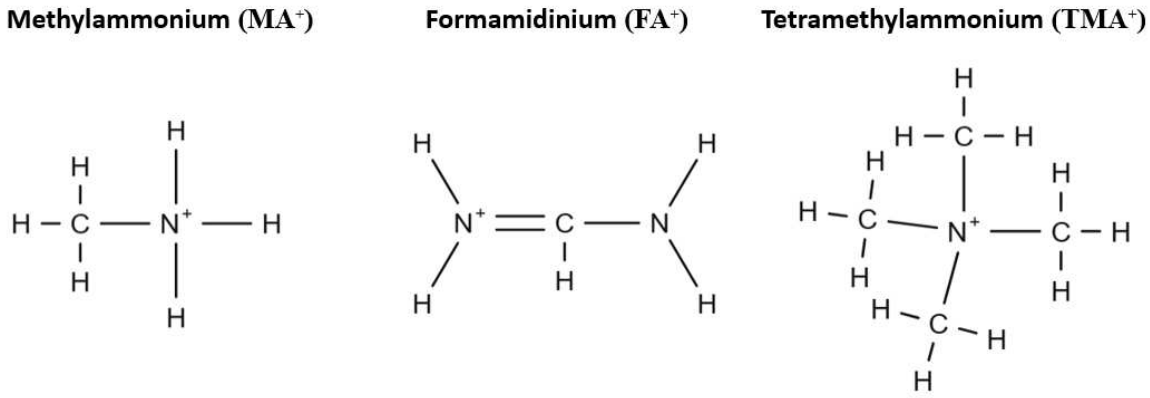

Source: Prepared by the author.

Despite the advances in tailoring the optical and electronic properties of hybrid perovskites, their practical application faces significant challenges, such as structural instability, chemical degradation, and environmental concerns related to the use of lead. Furthermore, the limited lifetime of solar cells and concerns over Pb leakage hinder their large-scale deployment. In response to these limitations, research has focused on developing more stable and less toxic perovskites, especially those employing Sn as a substitute for Pb. These materials retain electronic properties comparable to those of conventional perovskites, enabling similar applications in optoelectronic devices but with reduced environmental impact (FERJANI et al., 2025; LI et al., 2025).

3.2 Advances in Perovskite Solar Cells

Photovoltaic technology has emerged as a promising solution to meet the growing demand for clean and sustainable energy (LIANG et al., 2025). Commercial photovoltaic cells, currently based on silicon, offer high energy conversion efficiency and stability. However, their

manufacturing involves costly and complex processes, in addition to generating toxic byproducts. This scenario highlights the need for more sustainable, cost-effective, and efficient alternatives (ZHAO et al., 2023).

In this context, perovskite solar cells (PSCs) have advanced significantly in recent years, offering a promising alternative for the next generation of photovoltaic technology. With advances in preparation methods, the power conversion efficiency of PSCs has increased from an initial 3.6% to 26.7% over the past decade, approaching the efficiency of conventional crystalline silicon solar cells. Considering that PSC research began just over a decade ago, and that, in comparison, silicon solar cells took 70 years to reach efficiencies above 26%, the prospects for the future of PSCs are highly promising (LI et al., 2025; YANG et al., 2025).

Figure 7 presents the most recent power conversion efficiencies of solar cells, highlighting the progress of perovskite solar cells in recent years. Based on the latest data from NREL (2024), the graph compares the efficiencies of silicon, perovskite, and tandem solar cells, which combine perovskites with other photovoltaic materials.

Figure 7 – Evolution of the maximum conversion efficiencies of different solar cell technologies over time. The graph compares crystalline silicon cells (blue), emerging perovskites (red), and perovskite/silicon tandem structures (brown), highlighting the rapid progress of perovskites.

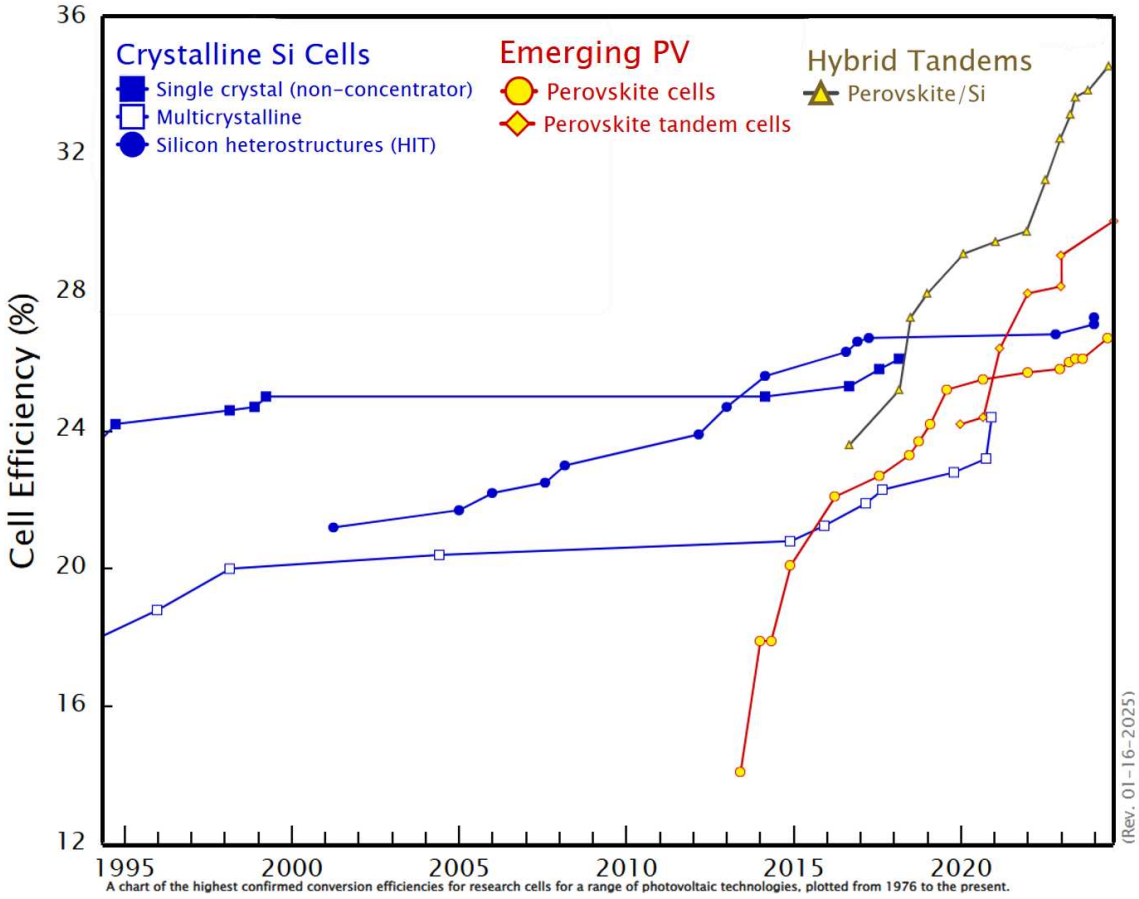

Source: NREL, 2025, adapted.

In addition to significant advances in power conversion efficiency, perovskites have drawn attention for their ability to be manufactured through simpler and more cost-effective processes. These materials can be processed at temperatures below 200 °C, using techniques such as solution processing or vapor deposition. In contrast, silicon requires manufacturing steps at high temperatures, around 1,000 °C, which substantially increases production costs. However, several issues still limit the performance and industrialization of perovskite solar cells, including layer defects, energy level mismatch, and, above all, chemical instability (LI et al., 2025; FIGUEREDO, 2022).

In this context, continuous efforts have been directed toward the development of new components, interface engineering, the inclusion of functional additives, and the design of

improved layers for PSCs. These strategies aim not only to address existing challenges but also to explore the full potential of these devices. PSCs combine high efficiency with lower costs and greater flexibility, features that make them viable for large-scale applications (LI et al., 2025).

The dimensionality of perovskites directly affects their physical, chemical, and optical properties. While three-dimensional (3D) perovskites present drawbacks such as a high density of surface defects and lower stability under adverse conditions, particularly in humid environments, at high temperatures, and under sunlight exposure, low-dimensional perovskites stand out for their greater structural stability and resistance to these factors. This difference is related to the separation between inorganic structural units, which reduces octahedral interaction and limits charge carrier delocalization. To enhance the stability of these compounds, a common strategy has been to reduce the dimensionality of 3D perovskites by introducing bulky organic cations that do not fit into the network of corner-sharing $[BX_6]^{4-}$ octahedra, favoring the formation of structures with edge- or face-sharing octahedra, or even arrangements of isolated octahedra organized in layers. Furthermore, these organic cations are generally hydrophobic, which helps mitigate moisture- and heat-induced degradation in devices such as PSCs (ZHAO et al., 2023; ZHOU et al., 2019).

Designing and constructing new perovskite-type structures based on organic cations suitable for occupying the A-site and/or coordinating halides and metals at the X and B sites, respectively, has been one of the main strategies for mitigating structural instability in hybrid perovskites and enhancing their properties (VASCONCELOS, 2023). Among these approaches, the use of aromatic spacers such as imidazoles at the A-site stands out. These spacers promote better organization between organic and inorganic layers, as well as facilitating the separation of electrons and holes generated by light absorption. This separation reduces the attractive force between these particles, resulting in a lower exciton binding energy and facilitating their dissociation. Consequently, improved charge transport and higher efficiency are observed in devices such as PSCs (HAN; CHENG; CUI, 2023; ZHOU et al., 2024).

Another approach is the replacement of Pb^{2+} ions with tetravalent metal ions (B^{4+}), such as Sn^{4+}, at the B-site, resulting in vacancy-ordered double perovskites with the general formula A_2BX_6. These structures belong to the class of zero-dimensional (0D) perovskites, characterized by isolated $[BX_6]$ octahedra separated by monovalent cations at the A-site, without direct corner-, edge-, or face-sharing. The use of tetravalent ions provides greater chemical stability, which increases device durability and contributes to the development of safer and more environmentally friendly materials (YANG et al., 2025). Compared to traditional

ABX_3-type perovskites (3D structure), A_2BX_6 variants exhibit superior stability under adverse environmental conditions, such as humidity, heat, and radiation. This higher stability is associated with the presence of tetravalent metal ions (B^{4+}), such as Sn^{4+}, which are less susceptible to oxidation than the divalent ions (B^{2+}) used in ABX_3. Moreover, the structure of A_2BX_6 consists of electronically and physically isolated $[BX_6]^{2-}$ octahedra, which reduces the propagation of structural defects and limits degradation caused by external agents (MAUGHAN et al., 2019; WU et al., 2025).

In addition to their structural stability, A_2BX_6 perovskites exhibit electronic characteristics typical of 0D materials, in which the $[BX_6]$ octahedra remain electronically isolated. This configuration promotes spatial confinement of charge carriers and contributes to the formation of self-trapped excitons (STE), a phenomenon associated with efficient radiative recombination. This mechanism, together with the separation between inorganic units, is directly related to the greater chemical stability observed in these systems (SHENG et al., 2024).

3.3 Physical Concepts

The electrical and optical properties of a crystalline solid, such as electrical conductivity and optical absorption, are intrinsically linked to its energy band structure. These bands result from the interaction and coupling between the energy levels of the constituent atoms, promoted by the crystal's periodic arrangement during solid formation. The configuration of the bands, in turn, depends directly on the crystal structure of the material, since the structure determines how the atomic orbitals interact within the solid. From a technological standpoint, the arrangement of the energy bands, particularly the energy gap between the lowest point of the conduction band and the highest point of the valence band, plays a decisive role in the material's electronic properties. This gap, known as the bandgap, determines the electrical conductivity and directly affects the optical characteristics, such as light absorption and emission (KITTEL, 2005; LAURETO et al., 2005).

In the field of optoelectronics, the bandgap is a key parameter for material functionality. By definition, semiconductors are materials that exhibit a forbidden band (bandgap) between the valence band and the conduction band, typically ranging from fractions of an electronvolt up to about 3 eV. This energy range allows electrical conduction under certain conditions, such as thermal or optical excitation (LAURETO et al., 2005). As the temperature increases, electrons are thermally excited from the valence band to the conduction band. Both

the electrons in the conduction band and the vacant orbitals or holes left behind in the valence band contribute to the material's electrical conductivity (KITTEL, 2005).

When characterizing a semiconductor material, it is important to determine whether the optical bandgap involves direct or indirect transitions, as this influences the charge carrier dynamics and their recombination after photoexcitation. In semiconductors with a direct bandgap, the transition between the valence band maximum (VBM) and the conduction band minimum (CBM) occurs at the same wave vector (same point in k-space). Since the photon has very little linear momentum, this transition can occur without significant variation in k, making it electric-dipole allowed. This favors efficient radiative recombination of electron–hole pairs. On the other hand, in semiconductors with an indirect bandgap, the VBM and CBM occur at different points in k-space, so the optical transition requires not only the absorption (or emission) of a photon but also the participation of a phonon to conserve crystal momentum. This requirement makes radiative recombination less likely, reducing photoactive efficiency compared to direct-gap materials (ANDRADE et al., 2024; KITTEL, 2005; YUAN et al., 2018).

It is worth noting that a direct bandgap allows electrons to emit photons directly when transitioning from the conduction band to the valence band, whereas an indirect bandgap requires an additional interaction with a phonon for this transition, as illustrated in the schematic of Figure 8 (SHENG et al., 2024).

Figure 8 – Schematic of (A) direct and (B) indirect bandgap transitions.

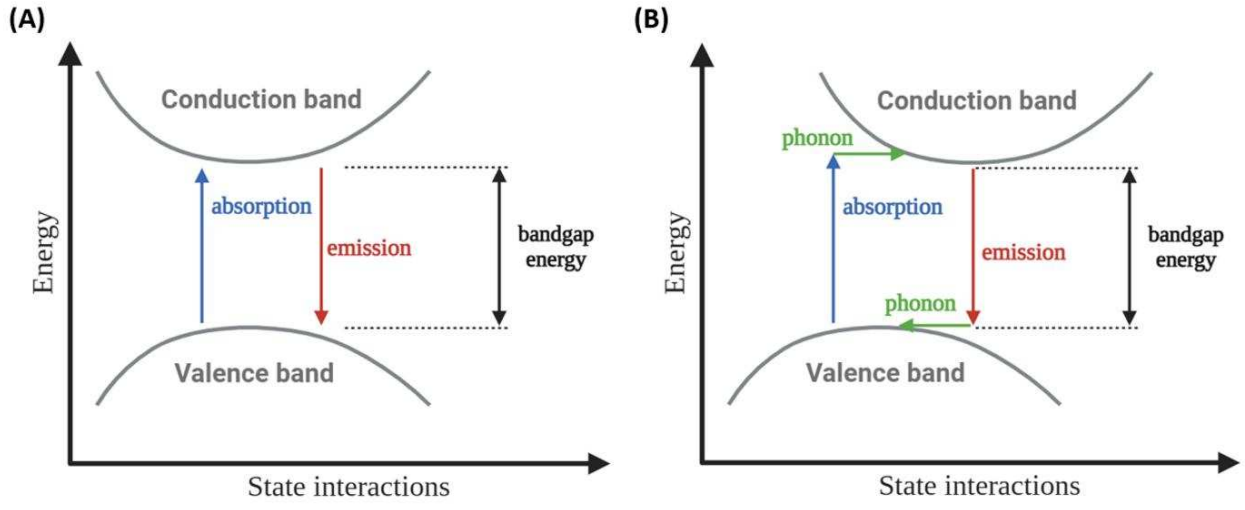

Source: Prepared by the author.

4 METHODOLOGY

4.1 Reagents

2-(1H-imidazol-1-yl)-1-phenylethanone ($C_{11}H_{10}N_2O$), hereinafter referred to as organic compound C1, synthesized according to Costa et al., 2021; hydrobromic acid (HBr, 48%, Dinâmica); tin(II) bromide ($SnBr_2$, 98%, Sigma-Aldrich); hypophosphorous acid (H_3PO_2, 50%, Sigma-Aldrich); and diethyl ether ($C_4H_{10}O$, 99.5%, Êxodo). All reagents used were of analytical grade and employed without prior treatment.

4.2 Synthesis and Purification of Crystals

Single crystals of $(C_{11}H_{11}N_2O)_2SnBr_6$ were obtained via the slow evaporation method in an acidic medium. The organic compound C1 (2-(1H-imidazol-1-yl)-1-phenylethanone) was used as a precursor in the synthesis of single crystals, having been previously synthesized as described in the literature by Costa et al., 2021.

For crystal preparation, 25 mg (0.134 mmol) of the organic compound ($C_{11}H_{10}N_2O$) were dissolved in 1 mL of concentrated hydrobromic acid under heating at 100 °C and constant stirring in a glass beaker. Simultaneously, a solution of 19 mg (0.068 mmol) of tin(II) bromide ($SnBr_2$) was prepared under the same conditions, using 1 mL of the same acid. Continuous stirring ensured complete dissolution of the reagents. After dissolution, the two solutions were gradually mixed, maintaining vigorous stirring to ensure homogeneity of the reaction mixture, as illustrated in Figure 9.

Immediately after mixing, 50 µL of hypophosphorous acid (H_3PO_2) were added to act as a reducing agent and help maintain the Sn^{2+} ion in solution under acidic conditions. However, due to the experimental conditions (high temperature, strongly acidic medium, and exposure to atmospheric oxygen), oxidation of Sn^{2+} to Sn^{4+} occurred, leading to the formation of the compound with tin in the +4 oxidation state. The overall reaction of the synthesis can be represented as follows:

$$2\ C_{11}H_{10}N_2O + 4\ HBr + SnBr_2 + \frac{1}{2}\ O_2 \rightarrow (C_{11}H_{11}N_2O)_2[SnBr_6] + H_2O$$

The solution was maintained under heating until its volume was reduced to half of the initial volume, resulting in the progressive concentration of the reagents, an essential condition to induce nucleation and sustain controlled crystal growth.

Once the desired volume was reached, the solution was removed from the heat source, labeled, and left to stand at room temperature for 72 h. During this period, the slow evaporation of the solvent resulted in a controlled crystallization process, allowing the formation of single crystals of $(C_{11}H_{11}N_2O)_2SnBr_6$ at the bottom of the container. This procedure yielded crystals of suitable size for structural analyses, exhibiting a light-yellow color and good transparency.

Figure 9 – Schematic of the synthesis procedure for single crystals of $(C_{11}H_{11}N_2O)_2SnBr_6$.

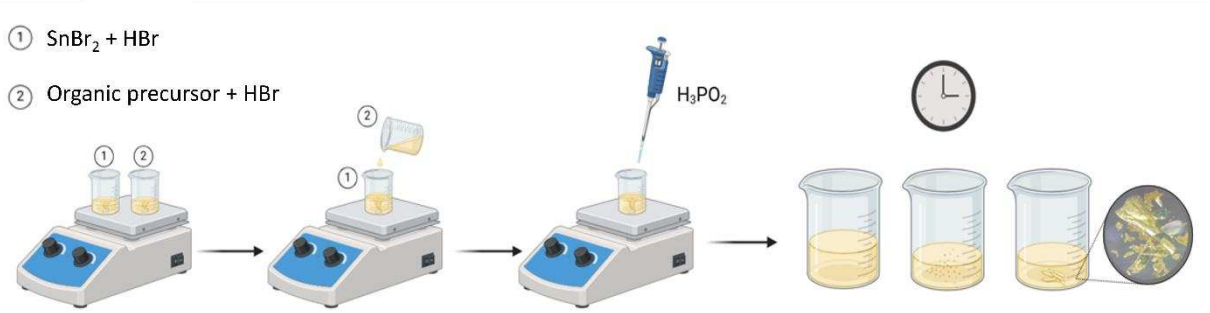

Source: Prepared by the author.

With the progressive evaporation of the solvent and the observation of crystal formation, the remaining liquid was carefully removed, and the crystals were subjected to successive washings with small portions of diethyl ether in order to eliminate possible surface impurities without compromising the integrity of the formed crystals. The single crystals were collected using an aluminum spatula, with careful handling to avoid damaging them.

After collection, the crystals were transferred to a desiccator, where they remained under controlled atmosphere conditions, protected from ambient humidity, until their use in subsequent analyses.

4.3 Characterization

The crystal structure was elucidated using single-crystal X-ray diffraction (SCXRD) measurements. Crystallographic data were collected at two temperatures, 100 K and 298 K, using different instruments. The details of both setups are described below.

The structural analysis of the $(C_{11}H_{11}N_2O)_2SnBr_6$ single crystal at 100 K was performed using the MANACA beamline diffractometer at LNLS-Sirius (Brazilian Synchrotron Light Laboratory), equipped with a PILATUS2M detector and a monochromatic X-ray source (0.67937 Å). Data were recorded in rotation mode using the ω-scan technique with 2θ_max = 57.2°, and data acquisition was performed using MXCuBE software (GABADINHO et al., 2010; OSCARSSON et al., 2019). The XDS program was used for data integration, and empirical absorption correction was applied. The crystal structure was solved with SHELXT, and refinement was conducted by full-matrix least squares against F^2 using SHELXL (SHARFALDDIN et al., 2020; SPACKMAN et al., 2021) through the Olex2 interface (DOLOMANOV et al., 2009; SHELDRICK, 2015).

The crystallographic information collected at 298 K was obtained using a Bruker D8 Venture X-ray diffractometer equipped with a Photon II CPAD detector and an Incoatec IμS 3.0 microfocus source of Mo Kα radiation (λ = 0.71073 Å). The crystal used in the study was selected and mounted on a MiTeGen MicroMount with the aid of immersion oil to ensure stability during experiments. Unit cell determination and data collection were performed using APEX 4 software. Data reduction and global unit cell refinement were carried out with the Bruker SAINT+ software package, while numerical absorption correction was performed with SADABS. Structure solution employed the intrinsic phasing method available in SHELXT, and structure refinement was performed by least-squares methods implemented in SHELXL, operated via the Olex2 graphical interface. The Vesta software (MOMMA; IZUMI, 2011) and CrystalExplorer (SPACKMAN et al., 2021) were used to prepare the graphical representations for this document.

Room-temperature absorption spectra were obtained by reflectance spectroscopy (DRS) using a Shimadzu UV-2600 spectrophotometer equipped with an ISR-2600 Plus integrating sphere, covering the spectral range from 200 to 800 nm. Reflectance data were subsequently converted into absorption spectra by applying the Kubelka–Munk function.

Low-temperature photoluminescence (PL) spectra and the Raman spectrum of the material were obtained using a Jobin-Yvon T64000 spectrometer equipped with an Olympus microscope and a liquid-nitrogen-cooled CCD detector. For Raman spectrum acquisition, a 633

nm laser was used as the excitation source, with measurements carried out at room temperature. For PL measurements, an external light source with a wavelength of 395 nm was employed. During the measurements, the sample was kept under vacuum inside a closed-cycle cryostat operated with compressed helium, ensuring low-temperature conditions. The system allowed precise temperature control, with stability of ±0.1 K.

Photoluminescence lifetime measurements were performed using a Horiba PPD-900 system equipped with a FiPho detector and a DeltaDiode 405 nm (DD-405L) laser excitation source. Decays were acquired for three different emission wavelengths (490 nm, 520 nm, and 735 nm) using the time-correlated single photon counting (TCSPC) method.

Fourier-transform infrared (FTIR) data were obtained using an ATR accessory, operating in attenuated total reflectance mode under vacuum to minimize interference from water and CO_2. Measurements were carried out with a Bruker Vertex 70 V spectrometer, with signals collected by pyroelectric DLaTGS detectors.

5 RESULTS AND DISCUSSION

5.1 Single-Crystal X-Ray Diffraction (SCXRD)

SCXRD analysis was employed to determine the crystal structure of the compound $(C_{11}H_{11}N_2O)_2SnBr_6$. The data obtained confirm the formation of a vacancy-ordered double hybrid perovskite, whose crystal structure contains isolated $[SnBr_6]^{2-}$ octahedra. As illustrated in Figure 10, part (A) shows the spatial arrangement of the constituents within the unit cell; part (B) depicts the fundamental structural unit formed by the octahedron and the associated organic cations; and part (C) presents the intermolecular distances between the centers of the $[SnBr_6]^{2-}$ octahedra, reinforcing the absence of direct connectivity between them.

The physical isolation of the $[SnBr_6]^{2-}$ octahedra leads to the formation of quantum wells within the structure. Although the material is classified as 0D, the organization of the inorganic and organic components establishes an arrangement in which charge carriers generated by optical excitation tend to remain localized around each octahedral unit.

In this configuration, the centers of the $[SnBr_6]^{2-}$ units are separated by an average distance of 12.1 Å, consistent with values reported for low-dimensional hybrid perovskites containing bulky cations. In materials such as $(PEA)_2SnBr_6$, for example, the separation between metal centers can exceed 1 nm (>10 Å), indicating effective octahedral isolation (Zhou et al., 2022). Such separation favors quantum confinement of charge carriers and the formation of STEs, due to the limited electronic coupling between octahedral units. Nevertheless, the observed distance still allows for restricted electronic migration between quantum wells, contributing to a balance between confinement and mobility, an important aspect for optoelectronic applications (AJAYAKUMAR et al., 2024).

Figure 10 – Crystal structure representation of the $(C_{11}H_{11}N_2O)_2SnBr_6$ perovskite at 100 K. (A) Unit cell; (B) Fundamental unit; (C) Inter-octahedral separations.

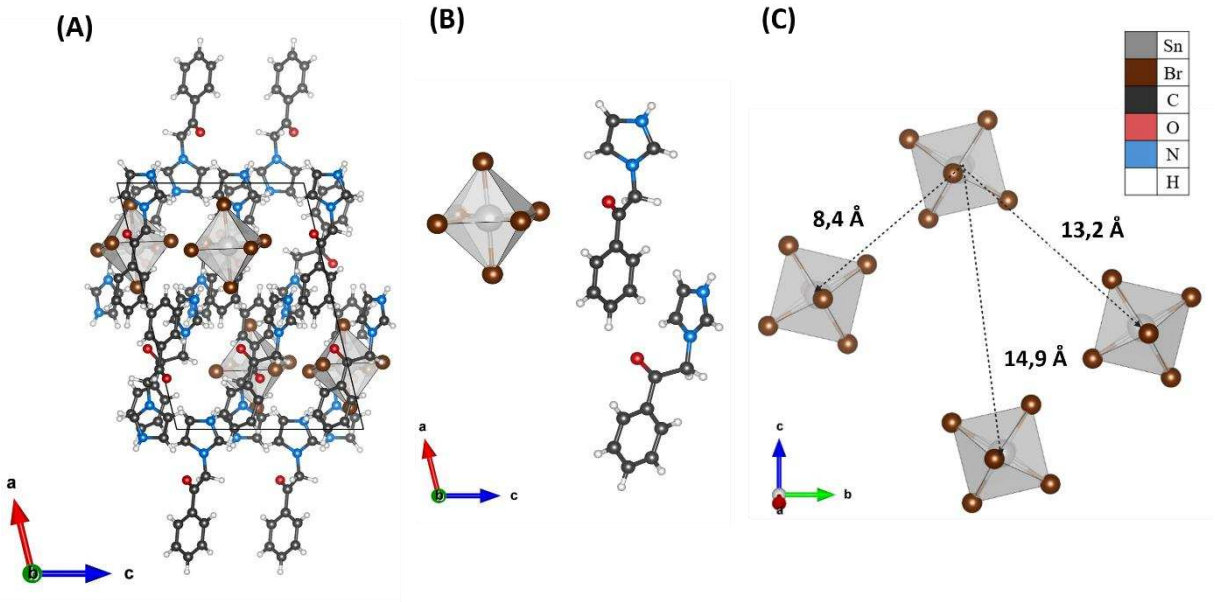

Source: Prepared by the author.

SCXRD analysis was conducted at two temperatures, 100 K and 298 K. In both measurements, it was verified that the compound crystallizes in a monoclinic system, with crystal symmetry described by the space group $P\ 2_1/c$, containing four formula units per unit cell (Z = 4) and the following crystallographic lattice parameters: a = 15.73400 Å, b = 16.49400 Å, c = 11.28200 Å, and β = 103.2580° at 100 K; and a = 15.8072 Å, b = 16.5829 Å, c = 11.4600 Å, and β = 103.3080° at 298 K. These data indicate that no phase transition occurs when varying the temperature within the range of 100 to 298 K. Table 1 provides a summary of the crystallographic data obtained and refined for the compound under study.

Table 1 – Crystallographic data of the sample obtained by SCXRD at 100 K and 298 K.

	$(C1)_2SnBr_6$_100K	**$(C1)_2SnBr_6$_298K**
Empirical formula	$C_{22}H_{22}Br_6N_4O_2Sn$	$C_{22}H_{22}Br_6N_4O_2Sn$
Formula weight	972.58	972.58
Temperature [K]	100	298
Crystal system	monoclinic	monoclinic
Space group (number)	$P2_1/c$ (14)	$P2_1/c$ (14)
a [Å]	15.734(2)	15.8072(4)
b [Å]	16.4940(13)	16.5829(4)
c [Å]	11.282(2)	11.4600(2)
α [°]	90	90
β [°]	103.258(7)	103.3080(10)
γ [°]	90	90
Volume [Å^3]	2849.8(8)	2923.33(11)
Z	4	4
ρ_{calc} [gcm^{-3}]	2.267	2.210
μ [mm^{-1}]	7.963	9.102
F(000)	1832	1832
Crystal colour	clear light colourless	clear light yellow
Crystal shape	block	block
Radiation	synchrotron (λ=0.67019 Å)	MoK_α (λ=0.71073 Å)
2Θ range [°]	3.42 to 60.05 (0.67 Å)	4.68 to 56.69 (0.75 Å)
Index ranges	-23 ≤ h ≤ 23	-21 ≤ h ≤ 21
	-24 ≤ k ≤ 24	-22 ≤ k ≤ 22
	-16 ≤ l ≤ 15	-14 ≤ l ≤ 15
Reflections collected	44628	85494
Independent reflections	8051	7276
	R_{int} = 0.0559	R_{int} = 0.0867
	R_{sigma} = 0.0376	R_{sigma} = 0.0418
Completeness	97.7 %	99.9 %
Data / Restraints / Parameters	8051/0/316	7276/0/317
Goodness-of-fit on F^2	1.044	1.049
Final R indexes	R_1 = 0.0346	R_1 = 0.0389
[$I \geq 2\sigma(I)$]	wR_2 = 0.0934	wR_2 = 0.0553
Final R indexes	R_1 = 0.0354	R_1 = 0.0863
[all data]	wR_2 = 0.0945	wR_2 = 0.0685
Largest peak/hole [eÅ^{-3}]	1.85/-1.39	1.01/-0.90
Extinction coefficient		0.00029(3)

Source: Prepared by the author.

The crystallographic data obtained confirm that the synthesized material is a low-dimensional hybrid perovskite belonging to the class of vacancy-ordered double perovskites. The structure crystallizes in the monoclinic system, and the refined bond lengths and angles reveal only small distortions of the $[SnBr_6]^{2-}$ octahedra compared to the ideal geometry (FOUDIA et al., 2025).

The unit cell volume of 2849.83 Å³ (at 100 K) and 2923.33 Å³ (at 298 K), combined with the multiplicity Z = 4, indicates a high density.

The variance of the bond angles was calculated using Equation 1, where α_n represents one of the internal angles of the octahedron considered in the analysis, all ideally close to 90°. This analysis resulted in a variance value $\sigma^2 = 1.533581°$, indicating a small deviation from the ideal geometry. Such low values suggest that the material preserves a well-defined octahedral geometry, with only minor angular variations.

$$\sigma^2 = \frac{1}{11}\sum_{i=1}^{12}(\alpha_i - 90)^2 \qquad \text{(Equation 1)}$$

Furthermore, the distortion index of the Sn–Br bonds was calculated using Equation 2, where d_i is the length of one of the six bonds between Sn and Br, and d_{mean} is the average bond length within the octahedron. The value obtained, D = 0.0062503 Å, reflects the uniformity of the chemical interactions between the central atom and the ligands. This finding corroborates the low angular distortion observed, reinforcing the notion that the $[SnBr_6]^{2-}$ octahedron is structurally well-ordered in this system.

$$D = \frac{1}{6}\sum_{i=1}^{6}\frac{|d_i - d_{méd}|}{d_{méd}} \qquad \text{(Equation 2)}$$

The calculated values are consistent with the crystallographic data available in the CIF file. In contrast to more distorted systems, such as certain three-dimensional perovskites or double perovskites with a higher degree of asymmetry, the structured and regular behavior of the studied perovskite suggests a more controlled impact of distortions on the material's electronic and optical properties.

In the case of the perovskite investigated in this work, the distortion of the $[SnBr_6]^{2-}$ octahedron is relatively low, as evidenced by the results obtained using Equations 1 and 2 provided below. This low distortion can be explained by the electronic configuration of the Sn^{4+} cation, which presents a filled d shell ([Kr] $4d^{10}$) and empty 5s and 5p orbitals. Since there are no partially occupied degenerate orbitals in the valence shell, the Jahn–Teller effect does not

occur. Consequently, the $[SnBr_6]^{2-}$ octahedron tends to maintain a geometry close to the ideal, with only small variations in bond angles and lengths.

5.1.1 Hirshfeld Surface

Hirshfeld surface analysis was employed to identify the intermolecular interactions that influence crystal packing, using SCXRD data processed with *CrystalExplorer* (DHAWAN et al., 2024; SHARFALDDIN et al., 2020; SPACKMAN et al., 2021; WANG et al., 2024).

Figure 11(A) shows the surface mapped using the *d*norm function, which applies a color scale to indicate the distances between atoms relative to the sum of their van der Waals radii: red regions (*d*norm negative) correspond to contacts shorter than the sum, while white (*d*norm = 0) and blue (*d*norm positive) areas represent contacts at approximately equal and greater distances, respectively (HIRSHFELD, 1977; SOMAN; SUJATHA; ARUNKUMAR, 2014; SPACKMAN; JAYATILAKA, 2009).

Figure 11 – (A) Hirshfeld mapping with H···Br interaction distances; (B) and (C) fingerprint plots of organic molecule I and II, respectively; (D) chemical structure of the organic spacer 2-(1H-imidazol-1-yl)-1-phenylethanone ($C_{11}H_{10}N_2O$).

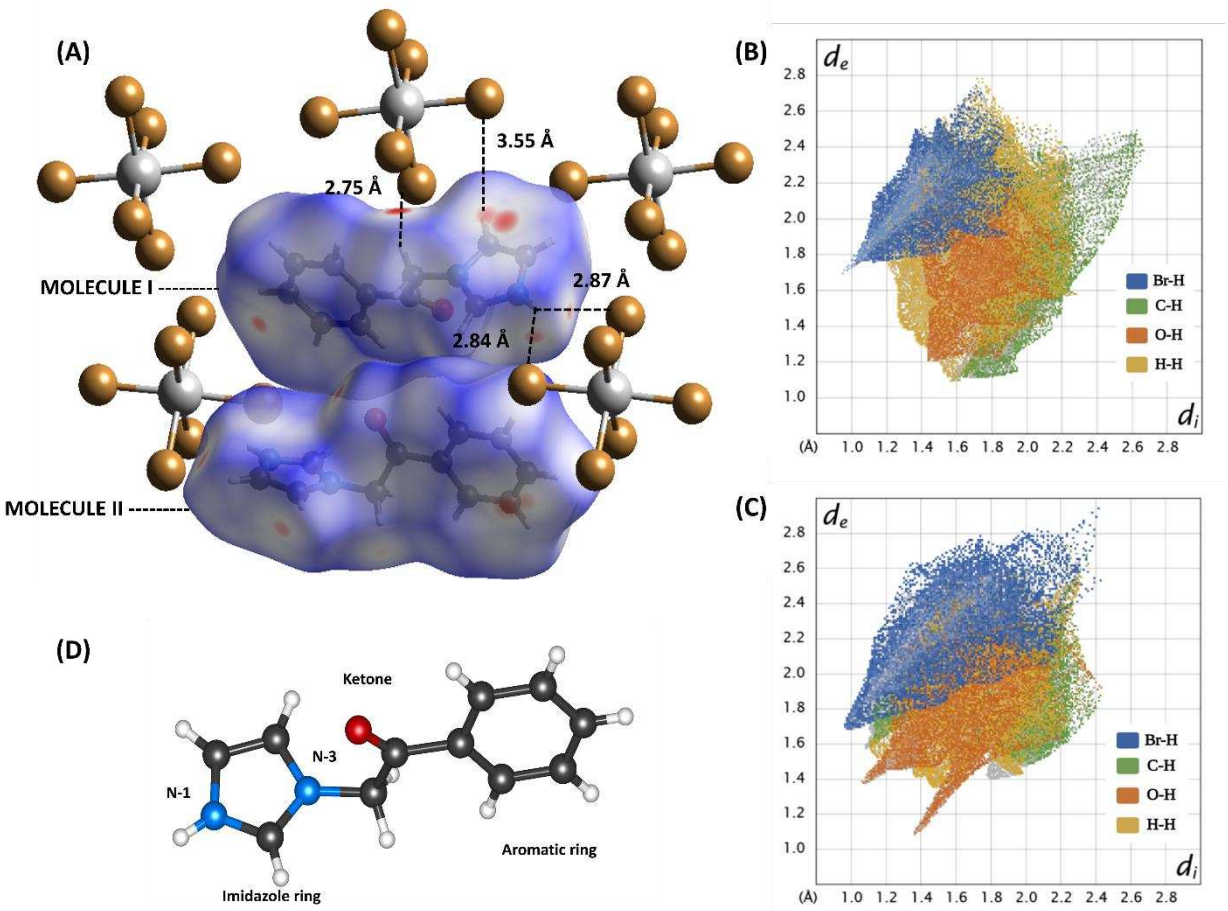

Source: Prepared by the author.

On the Hirshfeld surface, contacts with distances ranging from 2.75 Å to 2.87 Å suggest the presence of C–H···Br hydrogen-bond-type interactions, as they are shorter than the sum of the van der Waals radii of the atoms involved. In addition, N–H···Br interactions with distances of 2.87 and 2.84 Å were also observed, reinforcing the role of hydrogen bonds in stabilizing the crystal arrangement. In contrast, interactions with longer distances, such as 3.55 Å, indicate weaker hydrogen interactions (appearing on the Hirshfeld surface in a less intense red). These same contacts appear in the fingerprint plots [Figures 11(B) and 12(C)] as characteristic regions or “peaks,” allowing the specific contribution of Br···H to the crystal packing to be identified.

In the fingerprint plots, H···H interactions account for 35.9% and 25.3% for organic molecules I and II, respectively, whereas H···Br interactions account for 25.9% and 25.1%. These data suggest that the crystal lattice is predominantly stabilized by hydrogen bonds, as evidenced by the presence of peaks indicating these interactions.

The hydrogen atoms of the aromatic ring stand out in the formation of hydrogen bonds, as they are oriented to approach the Br atoms that form part of the octahedron. Although the molecule contains functional groups such as the ketone group and the imidazole ring, their participation in the interactions is distinct. The ketone group, despite being polar and electronegative, showed negligible contribution to interactions with the inorganic portion of the structure. This conclusion is corroborated by the fingerprint plots, which indicate a participation of only 0.2%, corresponding to interactions between the ketone oxygen and bromine atoms. Considering the spatial orientation and the type of interaction, it is more likely that the ketone group is involved in contacts with other organic molecules rather than directly with the $[SnBr_6]^{2-}$ octahedra.

On the other hand, the imidazole ring effectively participates in intermolecular interactions. In its structure, shown in Figure 11(D), nitrogen N-1, which has a relatively acidic hydrogen, acts as a hydrogen bond donor and participates in coordination interactions, increasing the complexity of the intermolecular network. Nitrogen N-3, however, lacking a lone electron pair, does not significantly contribute to the formation of such bonds (TOLOMEU; FRAGA, 2023).

Additionally, the aromatic ring not only provides the hydrogens responsible for bonding with the octahedra, but also, due to its conjugated system with delocalized π electrons, can engage in π–π interactions with other molecules, contributing to the formation of an ordered and cohesive network (JING et al., 2025).

In summary, this analysis confirms that the aromatic ring hydrogens play a key role as hydrogen bond donors, strongly contributing to the stabilization of the crystal packing. The imidazole ring, through the N-1 atom, also participates in intermolecular hydrogen bonds and coordination-type interactions, although its contribution is secondary compared to the aromatic hydrogens. In contrast, the ketone group shows negligible participation, with only minimal contacts detected in the Hirshfeld surface analysis.

5.2 Optical Properties

5.2.1 Diffuse Reflectance Spectroscopy (DRS)

To evaluate the optical properties, particularly with respect to the bandgap (*E*g) and light energy absorption, the crystals were characterized by diffuse reflectance spectroscopy (DRS).

The absorption spectrum, shown in Figure 12(A), displays three bands located at 5.2, 4.0, and 1.86 eV. The most pronounced valley, situated at 4.0 eV, was used, through analysis of the Tauc plot, to calculate the material's bandgap. For this, the reflectance data were converted using the Kubelka–Munk function, and the Tauc plot was constructed. As illustrated in Figure 12(B), the linear extrapolation of the ascending portion of the graph in the 4.0 eV region yielded a direct *E*g value of 2.99 eV.

Figure 12 – (A) Absorbance and PL spectra as a function of energy, where the blue line corresponds to the absorbance spectrum after treatment with the Kubelka–Munk equation; (B) Tauc plot for determining the optical bandgap.

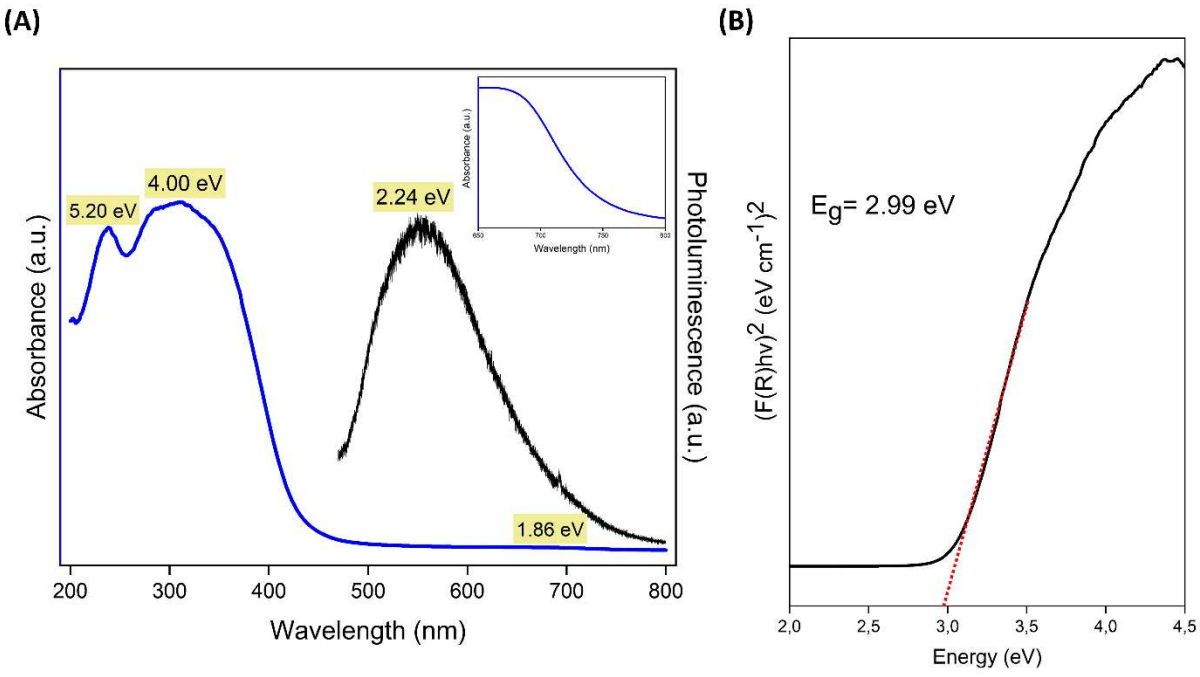

Source: Prepared by the author.

In previous studies, materials with similar compositions and structures exhibited bandgaps close to the values observed in this work. Soares et al. (2024) reported a bandgap of 3.16 eV in a perovskite also containing [$SnBr_6$] octahedra, while Ajayakumar et al. (2024) observed a value of 2.92 eV in a material with the same octahedron and a structurally similar organic moiety. These results indicate that vacancy ordering influences the bandgap width in perovskites of this class.

The band at 5.20 eV may be associated with interband electronic transitions related to defect states (such as vacancies or crystalline disorder), the presence of impurities in the material, or structural interactions, such as anisotropies in the electronic band structure that directly depend on crystal symmetry. Meanwhile, the band at 1.86 eV may be related to the formation of STEs, characteristic of low-dimensional materials, or to possible intraligand transitions in the organic cation, such as n–π or π–π transitions involving the orbitals of the imidazole ring or the ketone group (VASCONCELOS, 2023; YU; CARDONA, 2010).

The main absorption region lies between 200 and 400 nm, indicating that the perovskite has broad absorption in the ultraviolet region. This absorption is attributed to π–π^* transitions of the organic cation and to electronic transitions in the inorganic metal-halide framework (TURRO; RAMAMURTHY; SCAIANO, 2009).

Light absorption generates excited carriers, which can form excitons. The presence of excitons in perovskites is well-documented in the literature. The formation of self-trapped excitonic states depends on the dimensionality of the crystal system, being more favored in low-dimensional materials. In this context, reduced dimensionality facilitates exciton self-trapping, as the structure can confine these quasiparticles. This confinement is further reinforced by the dielectric contrast between the inorganic $[SnBr_6]^{2-}$ octahedral layers and the surrounding organic layers, which creates a potential barrier that limits charge screening. As a result, Coulomb interactions between electrons and holes are strengthened, favoring exciton stabilization and self-trapping (FERJANI et al., 2025; VASCONCELOS, 2023).

The large Stokes shift of 1.76 eV observed in the $(C_{11}H_{11}N_2O)_2SnBr_6$ crystals, a value practically identical to that of $(C_4N_2H_{14}Br)_4SnBr_6$ (1.73 eV) reported by Han et al. (2018), indicates strong electron–phonon coupling in the material. This behavior is characteristic of the formation of STEs, in which electronic excitation induces a local lattice distortion associated with phonon interaction. As a result, significant vibrational relaxation occurs before radiative emission, leading to a large energy difference between the absorption and emission bands. This separation between spectra reduces the overlap necessary for energy transfer between neighboring $[SnBr_6]^{2-}$ octahedra in the crystal lattice, making resonant excitation transport

inefficient. On the other hand, the confinement of excited states can be advantageous for optoelectronic applications, as it reduces non-radiative losses and favors spectrally well-defined emission (HAN et al., 2018).

5.2.2 Photoluminescence Spectroscopy (PL)

PL spectra analysis provides information on the thermal effects on carrier recombination processes in the studied material, contributing to the understanding of its electronic and optical properties (TURRO; RAMAMURTHY; SCAIANO, 2009).

Figure 13(A) shows the PL spectra obtained at temperatures ranging from 10 K to 300 K. The PL spectra at different temperatures, excited by a 395 nm laser, exhibit asymmetric and broad bands (approximately 1.6–2.6 eV). The PL emission center, corresponding to the most intense band, is located at 2.26 eV (approximately 549.78 nm).

The emission observed in the PL spectrum is associated with radiative recombination of charge carriers, including structural defects and, primarily, self-trapped excitons (STEs). In low-dimensional materials such as $(C_{11}H_{11}N_2O)_2SnBr_6$, the structure composed of isolated octahedra ensures the spatial confinement of excitons, leading to the formation of STEs. This process is reinforced by strong electron–phonon coupling, which induces local distortions in the crystal lattice, resulting in localization of the excited charge. Consequently, photoluminescent emission occurs with a large Stokes shift and in lower-energy regions, consistent with the low electronic levels associated with STEs (SHENG et al., 2024; YU et al., 2025).

Differences in PL profiles between high and low temperatures are related to the interaction between lattice thermal effects and electron–phonon interactions. At higher temperatures, increased phonon interactions favor non-radiative processes, resulting in a significant reduction in emission intensity, a phenomenon associated with thermal quenching, where excited charge carriers predominantly relax via non-radiative recombination (FOX, 2012; YU; CARDONA, 2010). In contrast, at lower temperatures, lattice relaxation facilitates electron–hole pair generation and promotes radiative emission from STE states, a behavior consistent with the observed PL spectra (GÓMEZ, 2023).

Furthermore, a shift of the main band toward lower energies, shown in Figure 13(C), is characteristic of semiconductor materials. This effect is observed, for example, in silicon solar cells, where the bathochromic shift (redshift) contributes to more efficient sunlight absorption, favoring applications in technologies such as thin films (YU; CARDONA, 2010).

Figure 13(D) presents the PL spectrum recorded at 10 K, whose fitting revealed two emission bands at 2.26 eV and 1.96 eV, characteristic of the STEs mentioned earlier, as indicated by the band widths (He et al., 2023). These STEs form due to strong electron–phonon coupling in the crystal lattice, which generates small structural distortions (or polarons), stabilizing the excitons in localized states under excitation (HAN; CHENG; CUI, 2023).

The analysis of temperature effects on PL focuses on the most intense band. Figures 13(B) and 13(C) show, respectively, the plots of full width at half maximum (FWHM) and the PL band center as a function of temperature. From these data, it is possible to extract the parameters of the phonons coupled to the excitons. Specifically, the fitting of FWHM versus temperature was performed using Equation 3, which describes the temperature dependence of the spectral broadening, allowing determination of the Huang–Rhys factor (S). This dimensionless parameter quantifies electron–phonon coupling, and the fitting resulted in S = 16.68 ± 0.19, a value similar to that reported for other low-dimensional perovskites (CHEN et al., 2024). In addition, a phonon energy of Eph = 0.043 eV was obtained, corresponding to approximately 346.8 cm^{-1}. This value is corroborated by analysis of the FTIR spectrum previously processed, shown in Figure 13(E), where a band at 348.8 cm^{-1} is observed, confirming phonon identification. Furthermore, the fitting parameters extracted from the PL band center versus temperature are summarized in Table 2, which highlights the extrapolated optical band gap at 0 K (E_0), the coupling constant (αph), and the effective phonon energy (Ee), along with the corresponding fitting statistics.

$$FWHM\ (T) = 2.36\sqrt{S}E_{ph}\left[coth\left(\frac{E_{ph}}{2kT}\right)\right]^{1/2} \qquad \text{(Equation 3)}$$

Table 2 – Parameters obtained from fitting the PL band center as a function of temperature for $(C_{11}H_{11}N_2O)_2SnBr_6$.

Parameter	Value	Standard Error	Description
E_0	1.9657	± 0.0068	Bandgap at 0 K
αph	0.2022	± 0.0935	Coupling constant
Ee	0.0133	± 0.0042	Effective phonon energy
Adj. R^2	0.942		Goodness of fit

χ^2 red	1.58×10^{-4}	Reduced Chi-square

Source: Prepared by the author.

Figure 13 – Evolution of PL spectroscopy with temperature; (A) PL spectrum, (B) FWHM as a function of temperature, and (C) PL band center position as a function of temperature, (D) PL spectrum fitting at 10 K, (E) processed FTIR spectrum, (F) Chromaticity coordinates as a function of temperature.

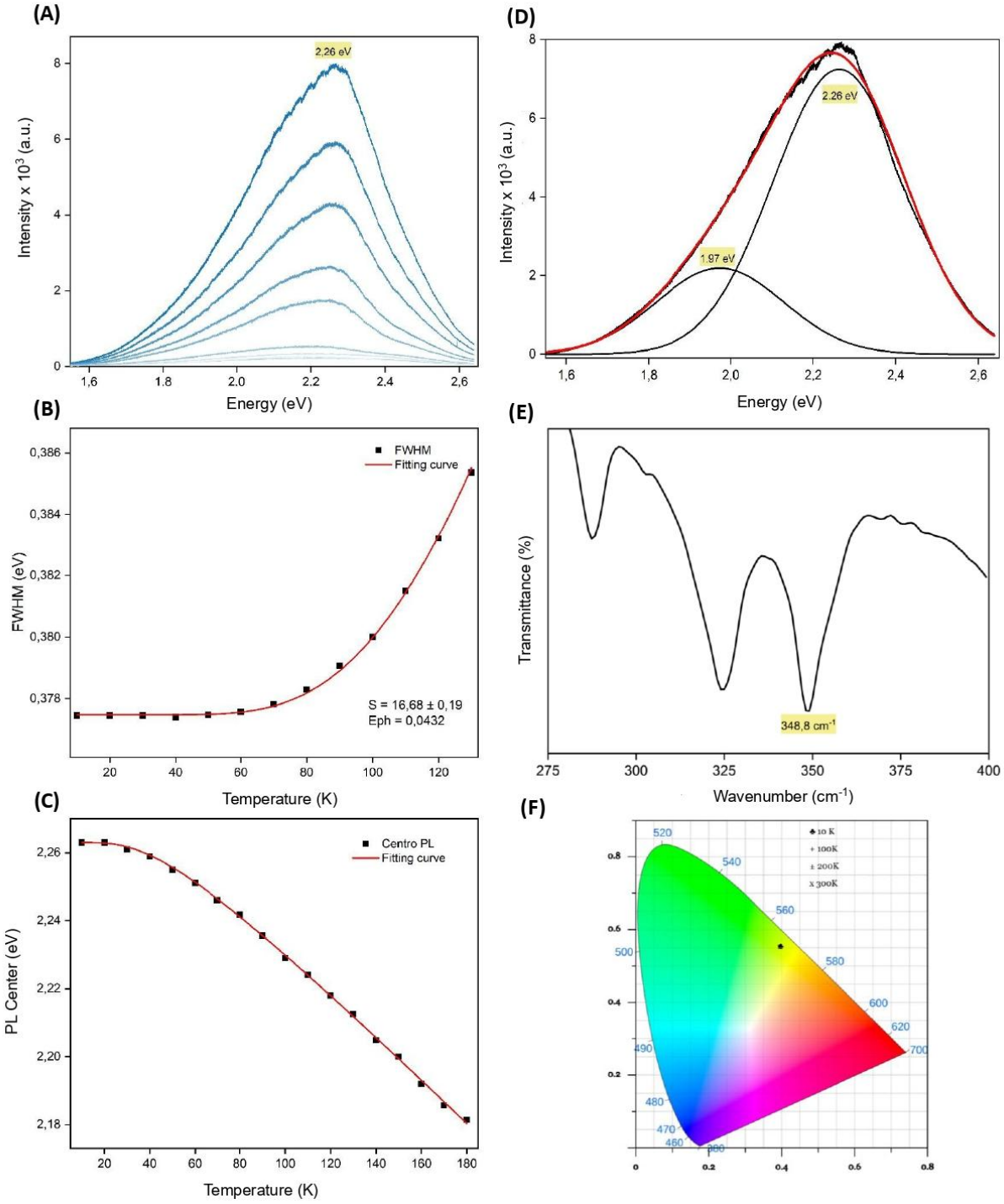

Source: Prepared by the author.

Another relevant aspect is the broadening of the PL band widths as the temperature increases. The broadening of the PL curve with increasing temperature is attributed to the intensified coupling between excitons and phonons, which causes both a shift in the energy of the emitted photons and the thermal broadening of the spectrum. In addition, at higher temperatures, excited vibronic states become accessible, increasing the diversity of energetic

transitions and contributing to the greater dispersion of emission energies. These combined factors result in the broadening observed in the PL curve (SOARES et al., 2024).

The emission of the synthesized crystals was also analyzed through the chromaticity coordinates of the International Commission on Illumination (CIE), obtained from the PL spectra. Figure 13(F) shows the variation of these coordinates as a function of temperature, indicating that the emission remains in the yellow-green region between 10 and 300 K. The stability of the coordinates suggests that the radiative recombination mechanism is not significantly affected by temperature, resulting in emissions with limited spectral variation. This behavior may be relevant for applications requiring color stability under different thermal conditions, such as in LEDs or displays (JOICY et al., 2025).

5.2.3 Photoluminescence Lifetime

The time-resolved photoluminescence decay curves of the $(C_{11}H_{11}N_2O)_2SnBr_6$ compound, monitored at the emission wavelengths of 490 nm [Figure 14(A)], 520 nm [Figure 15(B)], and 735 nm [Figure 14(C)], were fitted with a single-exponential decay, yielding characteristic lifetimes of τ_0 = 1.68 ns, 0.97 ns, and 0.73 ns, respectively. A clear reduction in τ_0 is observed with increasing emission wavelength, suggesting that emissions in lower-energy regions are associated with more relaxed excitonic states, with a higher probability of non-radiative recombination.

Figure 14 – Time-resolved photoluminescence decay curves of the $(C_{11}H_{11}N_2O)_2SnBr_6$ compound for emission wavelengths of 490 nm (A), 520 nm (B), and 735 nm (C).

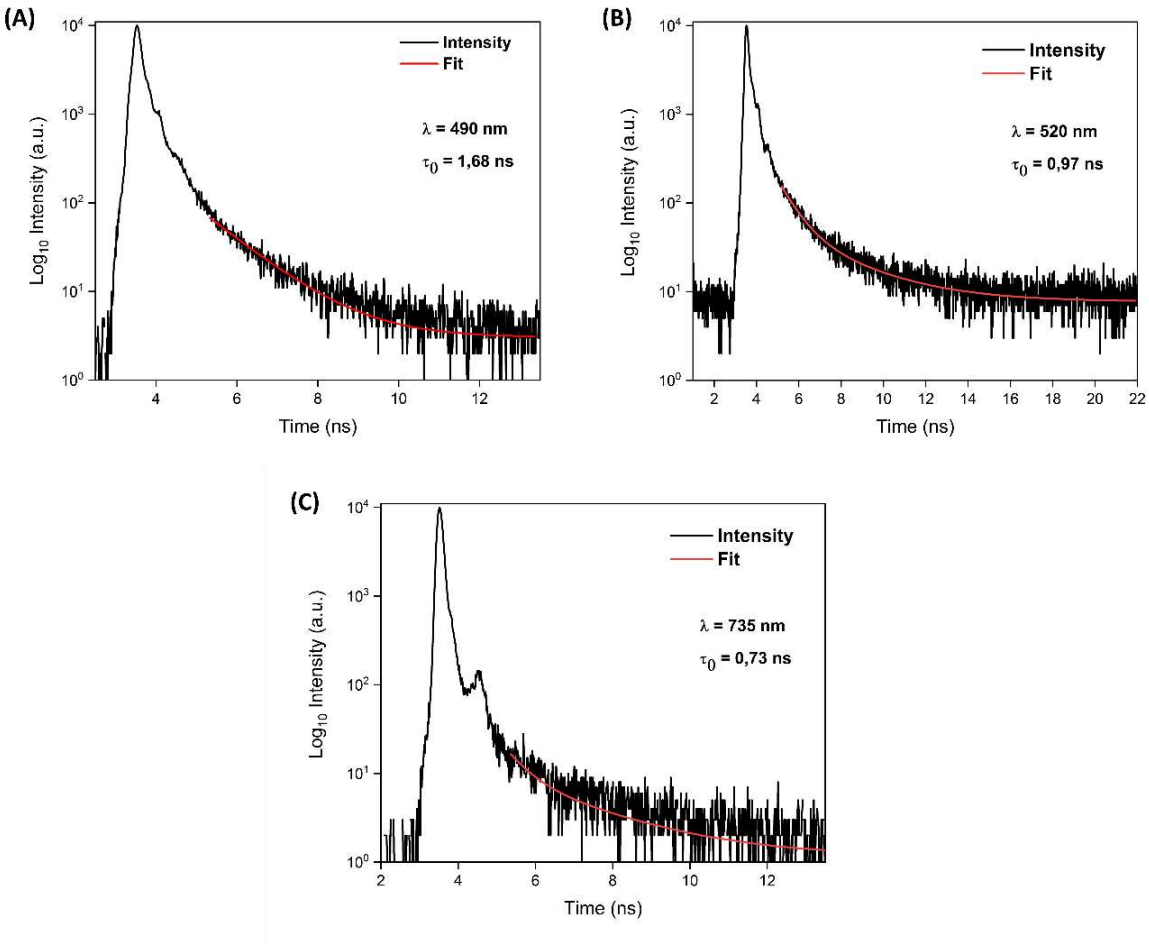

Source: Prepared by the author.

This behavior is consistent with the accelerated decay of STE processes in 0D perovskites. Bhaumik, Bruno, and Mhaisalkar (2020) reported that in similar 0D perovskites, PL lifetimes are in the nanosecond range, indicative of STE-dominated emission. In such confined structures, strong electron–phonon coupling drives exciton localization and rapid non-radiative relaxation, giving rise to shortened lifetimes compared to free exciton emission.

5.3 Vibrational Properties

5.3.1 Fourier Transform Infrared Spectroscopy (FTIR)

The vibrational investigation of the perovskite synthesized in this work was carried out using FTIR. Figure 15 presents a comparison between the spectrum of the organic precursor compound (C1) and the spectrum of the formed perovskite crystal, enabling the analysis of structural changes and chemical interactions that occurred during the synthesis.

Figure 15 – FTIR spectra of the organic compound and the perovskite containing the organic compound as part of its composition.

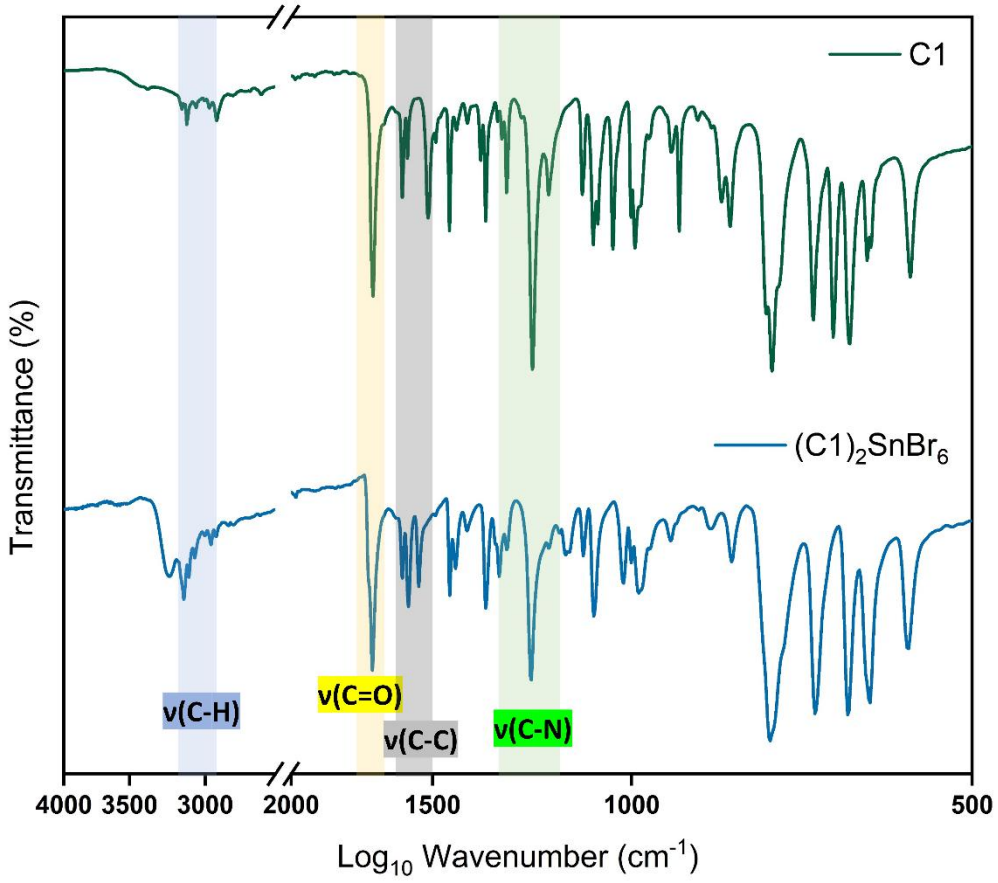

Source: Prepared by the author.

The FTIR spectrum of the organic compound (C1) exhibits characteristic bands of its functional groups: the carbonyl (C=O) band is located at 1695 cm^{-1}, the imidazole ring stretching (C–N) at 1217 cm^{-1}, and the aromatic vibrations (C–C) are observed at 1595, 1578, 1512, 1489, 1449, and 1427 cm^{-1}. The aromatic C–H stretching appears at 3113 cm^{-1} (University of Cincinnati, 2024). After the formation of the hybrid perovskite $(C1)_2SnBr_6$, slight

changes in these bands were observed. The carbonyl band remained at 1695 cm^{-1}, while the C–N stretching shifted to 1224 cm^{-1}. The aromatic C–H stretching exhibited a redshift, appearing at 3101 cm^{-1}, and the aromatic vibrations reorganized, with bands at 1596, 1575, 1542, 1448, and 1430 cm^{-1}.

The shift of the C–H band to a lower frequency suggests the presence of interactions between the hydrogen of the organic compound and bromine atoms in the inorganic structure (Pavia et al., 2021). The increase in the width and intensity of the band may indicate greater structural organization promoted by the integration of the organic compound into the perovskite. This hypothesis is corroborated by the Hirshfeld surface analysis, which shows close contacts between Br and H atoms.

5.3.2 Raman Spectroscopy

Figure 16 presents the Raman spectrum of the perovskite $(C_{11}H_{11}N_2O)_2SnBr_6$ at room temperature, under an excitation source of $\lambda_{ex}c$ = 514.5 nm (~2.4 eV). The analysis focused on characterizing the vibrational modes of the $[SnBr_6]^{2-}$ octahedron in the low-wavenumber region. In this spectrum, the intense bands in the range of 0–200 cm^{-1} are attributed to the vibrational modes of the octahedron and the translations of the organic cation. Additionally, the internal modes of $[SnBr_6]^{2-}$ appear near ~100 cm^{-1}, while a prominent band at ~216 cm^{-1} is related to contributions from the organic cations (Hernandez, 2019; Soares et al., 2024; Vasconcelos, 2023).

The band at 188 cm^{-1} is attributed to the symmetric stretching of Sn–Br bonds, while the bands at 137 cm^{-1} and 146 cm^{-1} correspond to asymmetric stretching, as described by Korobeynikov et al. (2022). Moreover, the band at 100 cm^{-1} is associated with the asymmetric bending Br–Sn–Br (Soares et al., 2024).

Figure 16 – Raman spectrum of the perovskite $(C_{11}H_{11}N_2O)_2SnBr_6$.

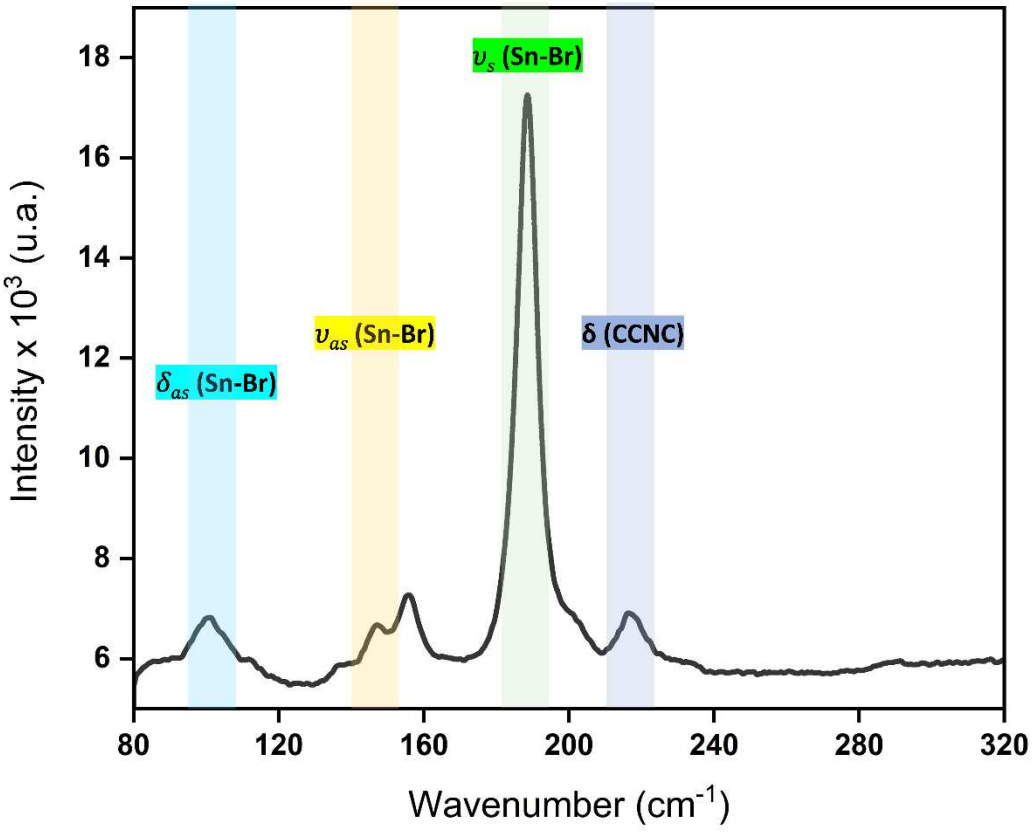

Source: Prepared by the author.

6 FINAL CONSIDERATIONS

In this work, the novel hybrid perovskite $(C_{11}H_{11}N_2O)_2SnBr_6$ was synthesized and characterized, and its structure was elucidated by single-crystal X-ray diffraction (SCXRD). Structural analysis revealed that the perovskite crystallizes in the monoclinic system, exhibiting isolated $[SnBr_6]^{2-}$ octahedra, characteristic of low-dimensional materials. Hirshfeld surface analysis and octahedral distortion assessment indicated that the structure is stable and only slightly distorted, favoring crystalline organization.

The DRS absorption spectra showed a main absorption region between 200 and 400 nm, with a bandgap determined at approximately 2.99 eV, a value consistent with materials of similar structure. The presence of interband electronic transitions suggests possible defect states or structural interactions that may influence its optical properties. PL analysis revealed emission centered at 2.26 eV, with thermal behavior characteristic of STEs, an effect intensified by the perovskite's low dimensionality and strong exciton–phonon coupling. Additionally, the shift of the main band as a function of temperature suggests significant coupling between electronic states and lattice vibrations.

Vibrational spectroscopy indicated the incorporation of the organic cation into the perovskite, evidenced by changes in the carbonyl and aromatic ring bands, while Raman spectra revealed the vibrations associated with the Sn–Br complex, confirming the preservation of the octahedral network.

The set of results obtained contributes to the understanding of the relationship between structure and optical properties of $(C_{11}H_{11}N_2O)_2SnBr_6$, highlighting its viability as an alternative to Pb-based perovskites. The achievement of a well-defined compound with favorable optical properties reinforces its potential for applications in optoelectronic devices. This study also advances the understanding of low-dimensional perovskites, paving the way for future investigations focused on optimizing their properties.

REFERENCES

ABDUR RAZZAQ, MD.; ISLAM, T. Optoelectronic study of double perovskite Rb_2SnBr_6: A first principles calculations. **Global Journal of Material Science and Engineering**, New Delhi, p. 1-5, 2020.

AJAYAKUMAR, A. *et al*. Zero-Dimensional Tin Halide Perovskite with Long Charge Carrier Lifetime and Anisotropic Photoconductivity for Selective Deep-UV Photodetection. **Advanced Functional Materials**, Weinheim, v. 34, n. 9, p. 2304899, 2024.

ANDRADE, P. H. M. *et al*. Band gap analysis in MOF materials: Distinguishing direct and indirect transitions using UV–vis spectroscopy. **Applied Materials Today**, Amsterdam, v. 37, p. 102094, 2024.

BHAUMIK, Saikat; BRUNO, Annalisa; MHAISALKAR, Subodh. Broadband emission from zero-dimensional Cs_4 PbI_6 perovskite nanocrystals. **RSC Advances**, Cambridge, v. 10, n. 23, p. 13431-13436, 2020.

BEECHER, A. N. *et al*. Direct Observation of Dynamic Symmetry Breaking above Room Temperature in Methylammonium Lead Iodide Perovskite. **ACS Energy Letters**, Washington, v. 1, n. 4, p. 880-887, 2016.

BECHTEL, J. S.; VAN DER VEN, A. Octahedral tilting instabilities in inorganic halide perovskites. **Physical Review Materials**, Maryland, v. 2, n. 2, p. 025401, 2018.

BUTLER, K. T. The chemical forces underlying octahedral tilting in halide perovskites. **Journal of Materials Chemistry C**, Cambridge, v. 6, n. 44, p. 12045-12051, 2018.

CHEN, C. *et al*. Bismuth (Bi3+) and Tellurium (Te4+) doped Cs2ZrCl6 lead-free halide perovskite phosphors for white LEDs. **Journal of Luminescence**, Amsterdam, v. 275, p. 120782, 2024.

COSTA, S. N. *et al*. Carbon steel corrosion inhibition in acid medium by imidazole-based molecules: Experimental and molecular modelling approaches. **Journal of Molecular Liquids**, Amsterdam, v. 326, p. 115330, 2021.

DALPIAN, G. M.; ZHAO, X.-G.; KAZMERSKI, L.; ZUNGER, A. Formation and composition-dependent properties of alloys of cubic halide perovskites. **Chemistry of Materials**, Washington, v. 31, n. 7, p. 2497-2506, 2019.

DHAWAN, P. *et al*. Diisopropylammonium hydrogen squarate: Synthesis and comprehensive analysis of non-linear optical co-crystal using X-ray, Hirshfeld, mechanical, optical and DFT methods. **Journal of Molecular Structure**, Amsterdam, v. 1318, p. 139197, 2024.

FERJANI, H. *et al*. Visible emission from a zero-dimensional tin-based organic-inorganic metal halide for luminescent devices: Experimental and theoretical investigation. **Journal of Molecular Structure**, Amsterdam, v. 1327, p. 141210, 2025.

FIGUEREDO, Larissa de S. Síntese e caracterização de filmes de perovskita híbrida orgânica-inorgânica de MAPbI3 contendo pontos quânticos de PbS para aplicação em sistemas

optoeletrônicos. 66p. Dissertação (Mestrado) – Programa de Pós Graduação em Ciência e Engenharia de Materiais (Área de Concentração: Materiais nanoestruturados), Universidade Tecnológica Federal do Paraná (UTFPR). Londrina, 2022.

FOUDIA, L. *et al*. A comprehensive theoretical investigation of the structural, elastic, electronic, optical, thermal, and catalytic properties of the monoclinic perovskite ScRhO3. **Materials Science in Semiconductor Processing**, Amsterdam, v. 185, p. 108853, jan. 2025.

FOX, M. **Optical properties of solids**. 2. ed., reprinted ed. Oxford: Oxford Univ. Press, 2012.

HIRSHFELD, F. L. Bonded-atom fragments for describing molecular charge densities. **Theoretica Chimica Acta**, Berlin, v. 44, p. 129-138, 1977.

GIORGI, G.; YAMASHITA, K. Organic–inorganic halide perovskites: an ambipolar class of materials with enhanced photovoltaic performances. **Journal of Materials Chemistry A**, Cambridge, v. 3, n. 17, p. 8981-8991, 2015.

GÓMEZ, Mayra Alexandra Padrón. **Exploring the structural and optical properties of low dimensional halide perovskite-like compounds at extreme conditions.** 2023. 106 f. Tese (Doutorado em Física) – Universidade Federal do Ceará, Fortaleza, 2023.

HAN, D. *et al.* Unraveling luminescence mechanisms in zero-dimensional halide perovskites. **Journal of Materials Chemistry C**, Cambridge, v. 6, n. 24, p. 6398-6405, 2018.

HAN, Y.; CHENG, X.; CUI, B.-B. Factors influencing self-trapped exciton emission of low-dimensional metal halides. **Materials Advances**, Cambridge, v. 4, n. 2, p. 355-373, 2023.

HE, Y. *et al.* Nature of self-trapped exciton emission in zero-dimensional Cs2ZrCl6 perovskite nanocrystals. **The Journal of Physical Chemistry Letters**, Washington, v. 14, n. 34, p. 7665-7671, 2023.

HERNANDEZ, Juan Simon Rodriguez. **Structural phase transitions on hybrid organic-inorganic halide perovskites based on bromide.** 2019. Dissertação (Mestrado em Física) – Universidade Federal do Ceará, Fortaleza, 2019.

HIRSHFELD, F. L. Bonded-atom fragments for describing molecular charge densities. **Theoretica Chimica Acta**, Berlin, v. 44, n. 2, p. 129-138, 1977.

JING, L. *et al.* Influence of π–π interactions on organic photocatalytic materials and their performance. **Chemical Society Reviews**, Cambridge, v. 54, n. 4, p. 2054-2090, 2025.

JOICY, S. *et al.* Synthesis, structural and optical characteristics of Mn and Ag co-doped ZnInS/ZnS core/shell nanocrystals: tunability of emission from orange to white for LED applications and flexible electronics devices. **Journal of Photochemistry and Photobiology A: Chemistry**, Amsterdam, v. 462, p. 116206, 2025.

INTERNATIONAL ENERGY AGENCY. **World Energy Outlook 2024.** Paris: IEA, 2024. Available at: https://www.iea.org/reports/world-energy-outlook-2024. Accessed on: Jan. 9, 2025.

KALTZOGLOU, A.; FALARAS, P. Recent developments on hybrid perovskite materials for solar energy conversion and environmental protection. **Current Opinion in Chemical Engineering**, Amsterdam, v. 33, p. 100708, 2021.

KARIM, M. M. S. *et al*. Anion distribution, structural distortion, and symmetry-driven optical band gap bowing in mixed halide Cs2SnX6 vacancy ordered double perovskites. **Chemistry of Materials**, Washington, v. 31, n. 22, p. 9430-9444, 2019.

KITTEL, C. **Introduction to solid state physics.** 8th ed. Hoboken: Wiley, 2005.

KOJIMA, A. *et al.* Organometal halide perovskites as visible-light sensitizers for photovoltaic cells. **Journal of the American Chemical Society**, Washington, v. 131, n. 17, p. 6050-6051, 2009.

KOROBEYNIKOV, N. A. *et al.* Bromine-rich tin(IV) halide complexes: experimental and theoretical examination of Br···Br noncovalent interactions in crystalline state. **Polyhedron**, Amsterdam, v. 222, p. 115912, 2022.

LAURETO, E. *et al.* A técnica de fotoluminescência aplicada à investigação de imperfeições estruturais em poços quânticos de materiais semicondutores. **Semina: Ciências Exatas e Tecnológicas**, Londrina, v. 26, n. 1, p. 23, 2005.

LI, Y. *et al.* MXene-based materials for efficient applications in perovskite solar cells: a review. **Journal of Materials Science & Technology**, Amsterdam, v. 215, p. 214-232, 2025.

LIANG, Q. *et al.* Highly stable perovskite solar cells with 0.30 voltage deficit enabled by a multi-functional asynchronous cross-linking. **Nature Communications**, London, v. 16, n. 1, p. 190, 2025.

LIN, K. *et al.* Perovskite light-emitting diodes with external quantum efficiency exceeding 20 per cent. **Nature**, London, v. 562, n. 7726, p. 245-248, 2018.

LIU, P. *et al.* High-quality Ruddlesden-Popper perovskite film formation for high-performance perovskite solar cells. **Advanced Materials**, Weinheim, v. 33, n. 10, p. 2002582, 2021.

LIU, T. *et al.* Solution-processed thin film transparent photovoltaics: present challenges and future development. **Nano-Micro Letters**, Singapore, v. 17, n. 1, p. 49, 2025.

MA, Q. *et al.* Solvents incubated π-π stacking in hole transport layer for perovskite-silicon 2-terminal tandem solar cells with 27.21% efficiency. **Journal of Energy Chemistry**, Amsterdam, v. 82, p. 25-30, 2023.

MANACÁ – LNLS. Available at: https://www.cnpem.br. Accessed on: Aug. 16, 2024.

MARCHENKO, E. I. *et al*. Relationships between distortions of inorganic framework and band gap of layered hybrid halide perovskites. **Chemistry of Materials**, Washington, v. 33, n. 18, p. 7518-7526, 2021.

MAUGHAN, A. E.; GANOSE, A. M.; SCANLON, D. O.; NEILSON, J. R. Perspectives and

design principles of vacancy-ordered double perovskite halide semiconductors. **Chemistry of Materials**, Washington, v. 31, n. 24, p. 8704-8721, 2019.

MCKINNON, J. J.; SPACKMAN, M. A.; MITCHELL, A. S. Novel tools for visualizing and exploring intermolecular interactions in molecular crystals. **Acta Crystallographica Section B: Structural Science**, Copenhagen, v. 60, n. 6, p. 627-668, 2004.

MIAH, M. H. *et al.* Band gap tuning of perovskite solar cells for enhancing the efficiency and stability: issues and prospects. **RSC Advances**, Cambridge, v. 14, n. 23, p. 15876-15906, 2024.

OU, T. *et al.* Rb2PtX6 (X = I, Br, Cl) vacancy-ordered double perovskites: effect of halogens on the structural, electronic, and optical properties. **Solid State Communications**, Amsterdam, v. 370, p. 115228, 2023.

PAVIA, D. L. *et al.* **Introduction to spectroscopy.** 5th ed. Boston: Cengage Learning, 2021.

PV MAGAZINE BRASIL. A mudança de energia mais rápida da história continua. **PV Magazine Brasil**, São Paulo, 2025. Available at: https://www.pv-magazine-brasil.com/2025/01/14/a-mudanca-de-energia-mais-rapida-da-historia-continua/. Accessed on: Jan. 15, 2025.

RAINA, P. *et al.* A review on stannate perovskites-based heterojunctions and their applications in the development of sustainable technologies and materials. **Materials Science in Semiconductor Processing**, Amsterdam, v. 188, p. 109224, 2025.

ROCHA, E. *et al.* Funcionalização de ligações C-H em estágio tardio em síntese orgânica. **Química Nova**, São Paulo, 2023.

SAPAROV, B.; MITZI, D. B. Organic-inorganic perovskites: structural versatility for functional materials design. **Chemical Reviews**, Washington, v. 116, n. 7, p. 4558-4596, 2016.

SHARFALDDIN, A. *et al.* Single crystal, Hirshfeld surface and theoretical analysis of methyl 4-hydroxybenzoate, a common cosmetic, drug and food preservative—experiment versus theory. **PLOS ONE**, San Francisco, v. 15, n. 10, p. e0239200, 2020.

SHENG, M. *et al.* Accelerated discovery of halide perovskite materials via computational methods: a review. **Nanomaterials**, Basel, v. 14, n. 13, p. 1167, 2024.

SMITH, M. D.; KARUNADASA, H. I. White-light emission from layered halide perovskites. **Accounts of Chemical Research**, Washington, v. 51, n. 3, p. 619-627, 2018.

SHI, H. *et al.* Mechanism of pressure-modulated self-trapped exciton emission in Cs2TeCl6 double perovskite. **Small**, Weinheim, v. 20, n. 48, p. 2405692, 2024.

SOARES, C. C. S. *et al.* Strong electron-phonon coupling in vacancy-ordered Cs2SnBr6 double perovskite. **Journal of Materials Chemistry C**, Cambridge, v. 12, n. 41, p. 16758-16765, 2024.

SOMAN, R.; SUJATHA, S.; ARUNKUMAR, C. Quantitative crystal structure analysis of fluorinated porphyrins. **Journal of Fluorine Chemistry**, Amsterdam, v. 163, p. 16-22, 2014.

SPACKMAN, M. A.; JAYATILAKA, D. Hirshfeld surface analysis. **CrystEngComm**, Cambridge, v. 11, n. 1, p. 19-32, 2009.

SPACKMAN, M. A.; MCKINNON, J. J. Fingerprinting intermolecular interactions in molecular crystals. **CrystEngComm**, Cambridge, v. 4, n. 66, p. 378-392, 2002.

SPACKMAN, P. R. *et al.* CrystalExplorer: a program for Hirshfeld surface analysis, visualization and quantitative analysis of molecular crystals. **Journal of Applied Crystallography**, Copenhagen, v. 54, n. 3, p. 1006-1011, 2021.

STOUMPOS, C. C. *et al.* Ruddlesden-Popper hybrid lead iodide perovskite 2D homologous semiconductors. **Chemistry of Materials**, Washington, v. 28, n. 8, p. 2852-2867, 2016.

SU, B. *et al.* Synthesis, crystal structure and green luminescence in zero-dimensional tin halide (C8H14N2)2SnBr6. **Inorganic Chemistry**, Washington, v. 59, n. 14, p. 9962-9968, 2020.

TOLOMEU, H. V.; FRAGA, C. A. M. Imidazole: synthesis, functionalization and physicochemical properties of a privileged structure in medicinal chemistry. **Molecules**, Basel, v. 28, n. 2, p. 838, 2023.

TURRO, N. J.; RAMAMURTHY, V.; SCAIANO, J. C. **Principles of molecular photochemistry: an introduction.** Sausalito: University Science Books, 2009.

UNITED NATIONS. **Renewable energy – powering a safer future.** Available at: https://www.un.org/en/climatechange/raising-ambition/renewable-energy. Accessed on: Jan. 9, 2025.

UNIVERSITY OF CINCINNATI. **Typical IR absorption frequencies for common functional groups.** Available at: https://chemed.chem.purdue.edu/genchem/topicreview/bp/2organic/infrared.html. Accessed on: Dec. 15, 2024.

VARSHNI, Y. P. Temperature dependence of the energy gap in semiconductors. **Physica**, Amsterdam, v. 34, n. 1, p. 149-154, 1967.

VASCONCELOS, F. N. F. **Perovskitas híbridas de haleto sob condições extremas de pressão e temperatura.** 2023. 110 f. Tese (Doutorado em Física) – Centro de Ciências, Universidade Federal do Ceará, Fortaleza, 2023.

VASHISHTHA, P. *et al.* High efficiency blue and green light-emitting diodes using Ruddlesden-Popper inorganic mixed halide perovskites with butylammonium interlayers. **Chemistry of Materials**, Washington, v. 31, n. 1, p. 83-89, 2019.

WANG, Q.; WANG, L. Renewable energy consumption and economic growth in OECD countries: a nonlinear panel data analysis. **Energy**, Amsterdam, v. 207, p. 118200, 2020.

WANG, W. *et al.* Rational design of 2D metal halide perovskites with low congruent melting temperature and large melt-processable window. **Journal of the American Chemical Society**, Washington, v. 146, n. 13, p. 9272-9284, 2024.

WU, Y. *et al.* Diverse carrier mobilities in halide perovskites: the role of conductive network and ionized impurity scattering. **Journal of Materials Science & Technology**, Amsterdam, v. 204, p. 245-254, 2025.

YAN, L. *et al.* Non-covalent interactions involving π effect between organic cations in low-dimensional organic/inorganic hybrid perovskites. **Applied Physics Letters**, Melville, v. 122, n. 24, p. 240501, 2023.

YANG, X. *et al.* Thermodynamic stability descriptor of A2BX6-type perovskite materials. **Materials Chemistry and Physics**, Amsterdam, v. 333, p. 130324, 2025.

YU, J. *et al.* Fluorine-expedited nitridation of layered perovskite Sr2TiO4 for visible-light-driven photocatalytic overall water splitting. **Nature Communications**, London, v. 16, n. 1, p. 361, 2025.

YUAN, L.-D. *et al.* Unified theory of direct or indirect band-gap nature of conventional semiconductors. **Physical Review B**, College Park, v. 98, n. 24, p. 245203, 2018.

YU, P. Y.; CARDONA, M. **Fundamentals of semiconductors: physics and materials properties.** Berlin: Springer, 2010.

ZANNATUL ARIF, M.; ZHOU, G. Design and numerical investigation of Cs2SnI6 vacancy-ordered double perovskite solar cell. **Optics & Laser Technology**, Amsterdam, v. 181, p. 111820, 2025.

ZHAO, Y. *et al.* Beyond two-dimension: one- and zero-dimensional halide perovskites as new-generation passivators for high-performance perovskite solar cells. **Journal of Energy Chemistry**, Amsterdam, v. 83, p. 189-208, 2023.

ZHONG, Y. *et al.* Collaborative strengthening by multi-functional molecule 3-thiophenboric acid for efficient and stable planar perovskite solar cells. **Chemical Engineering Journal**, Amsterdam, v. 436, p. 135134, 2022.

ZHOU, C. *et al.* Low dimensional metal halide perovskites and hybrids. **Materials Science and Engineering: R: Reports**, Amsterdam, v. 137, p. 38-65, 2019.

ZHOU, C. *et al.* Recent advances in luminescent zero-dimensional organic metal halide hybrids. **Advanced Optical Materials**, Weinheim, v. 9, n. 18, p. 2001766, 2021.

ZHOU, Y. *et al.* Aromatic imidazole diammonium-based 2D Dion-Jacobson perovskites with reduced exciton binding energy. **Advanced Functional Materials**, Weinheim, v. 34, n. 48, p. 2408774, 2024.